

# $K^\pm$ Production in Semi-Inclusive Deep Inelastic Scattering using Transversely Polarized Targets and the SoLID Spectrometer

(A Run-Group Proposal Submitted to PAC 46)

June 2, 2018

John Arrington, Whitney Armstrong, Paul Reimer, Seamus Riordan, Junqi Xie, Zhihong Ye<sup>\*†</sup>  
*Argonne National Laboratory, Physics Division, Argonne, IL, USA*

Andrew J. R. Puckett  
*University of Connecticut, Storrs, Connecticut, USA*

Haiyan Gao, Xiaqing Li, Weizhi Xiong, Xuefei Yan, Zhiwen Zhao<sup>\*</sup>  
*Duke University, Durham, NC, USA*

Fatiha Benmokhtar  
*Duquesne University, Pittsburgh, PA USA*

Alexandre Camsonne, Jian-Ping Chen, Tianbo Liu<sup>\*</sup>  
*Jefferson Lab, Newport News, VA, USA*

Miha Mihovilovič, Simon Širca  
*Faculty of Mathematics and Physics, University of Ljubljana, Slovenia*

Mitra H. Shabestari  
*Mississippi State University, Starkville, MS, USA*

Mohammad Hattawy  
*Old Dominion University, Norfolk, VA, USA*

Garth Huber  
*University of Regina, Regina, SK, Canada*

Abhay Deshpande, Klaus Dehmel, Nils Feege, Thomas Hemmick,  
Krishna Kumar, Sanghwa Park<sup>\*</sup>, Jinlong Zhang  
*Stony Brook University, Stony Brook, NY, USA*

Chendi Shen, Fuyue Wang, Yi Wang<sup>\*</sup>  
*Tsinghua University, Beijing, China*

1

---

<sup>1\*</sup>: Cospokespeople, †: Contact (yez@jlab.org, yez@anl.gov)

## Abstract

1

2

3 We propose to perform the measurement of the  $K^\pm$  production in the Semi-Inclusive Deep Inelastic Scattering  
4 (SIDIS) using both the transversely polarized proton ( $\text{NH}_3$ ) target and the transversely polarized  $^3\text{He}$  target  
5 (as effective polarized neutron target) on the SoLID spectrometer. This measurement will be carried out  
6 in parallel with the already approved SoLID experiments which will measure the  $\pi^\pm$  production in SIDIS,  
7 including E12-10-006 with a transversely polarized  $^3\text{He}$  target and E12-11-108 with a transversely polarized  
8  $\text{NH}_3$  target. We will perform the off-line analysis to extract the  $K^\pm$  Collins asymmetries, Sivers asymmetries  
9 and other TMD asymmetries. Model estimation shows that at the SoLID kinematic about 20% of the kaon  
10 SIDIS events come from the current fragmentation region where the TMD factorization can be applied. New  
11 data from this measurement will provide not only important input to determine the TMD of  $u$  and  $d$  quarks  
12 by combining with the pion measurements from SoLID and elsewhere, but also has the unique sensitivity to  
13 sea quarks. Our measurement will have a strong contribution to the development of the TMD physics and  
14 provide important guidance for studying sea-quark and gluon TMDs on future EIC.

15 This run group proposal does not need additional beam-time nor requires modification to the existing  
16 experiment design. The heavy-gas Čerenkov detector and the MRPC in the standard SIDIS setup already  
17 have the capability of identifying kaons from pions and protons at certain momentum ranges. We hope to  
18 improve the MRPC's time resolution down to 20 ps which should provide precise time-of-flight information  
19 for better  $\pi^\pm/K^\pm$  separation up to a high hadron momentum (e.g.  $P_h < 7.0 \text{ GeV}/c$ ). In this proposal, we  
20 will demonstrate that such a requirement is achievable in today's detector technologies.

# 21 Contents

22	<b>1 Physics motivation</b>	<b>4</b>
23	1.1 Transverse Momentum Dependent Parton Distributions (TMD) . . . . .	4
24	1.2 TMDs in Kaon SIDIS Production . . . . .	6
25	1.3 Spin asymmetries in SIDIS . . . . .	9
26	1.4 SIDIS kinematic regions . . . . .	11
27	<b>2 Experimental Setup</b>	<b>14</b>
28	<b>3 Kaon Identification</b>	<b>16</b>
29	3.1 Overview . . . . .	16
30	3.2 Pion rejection by HGC Detector . . . . .	17
31	3.3 Time-Of-Flight PID . . . . .	18
32	3.4 MRPC Detector . . . . .	19
33	3.5 Recent MRPC R&D Progresses . . . . .	19
34	3.6 MRPC Simulation Framework . . . . .	21
35	3.7 Kaon Identification with TOF and HGC . . . . .	24
36	<b>4 Projected Results</b>	<b>25</b>
37	4.1 Kinematic Coverage . . . . .	25
38	4.2 Rate Estimations . . . . .	31
39	4.3 Projected Asymmetries . . . . .	32
40	4.4 Systematic Uncertainties . . . . .	38
41	<b>5 Summary</b>	<b>38</b>

# 1 Physics motivation

Quantum chromodynamics (QCD) is nowadays viewed as the fundamental theory of strong interaction in the framework of Yang-Mills gauge theory. Unveiling the nucleon structure in terms of quarks and gluons is one of the main goals of nuclear and particle physics. Due to the nonperturbative nature of QCD at low energy scale, *e.g.* the hadron scale, a first principle calculation of nucleon structures is still a challenging issue. Several theoretical methods, such as the Euclidean lattice gauge theory [1], the Dyson-Schwinger equation [2], and the gauge/gravity duality [3], are developed to study the nonperturbative properties of QCD. Experimental tests will be essential to help us understand the nonperturbative dynamics of the strong interaction.

## 1.1 Transverse Momentum Dependent Parton Distributions (TMD)

Parton distribution functions (PDFs), which at the leading twist are interpreted as the probability density of finding a parton (quark or gluon) carrying the momentum fraction  $x$  at a resolution scale  $Q$ , are proven powerful tools in describing the inclusive deep inelastic scattering (DIS) process, the Drell-Yan process, and other high energy scattering processes. With the (collinear) factorization theorem, the cross sections of these high energy hadronic scattering processes can be expressed up to some power suppressed correction terms as a convolution of a process dependent but perturbative calculable partonic hard scattering part and process independent functions, *e.g.* PDFs, which encode the structure of a hadron. As a generalization of collinear PDFs, transverse momentum dependent parton distributions (TMDs) and generalized parton distributions (GPDs) are introduced to have three-dimensional descriptions of partonic structures of the nucleon. TMDs, which at the leading twist could be interpreted as a three-dimensional momentum distributions of the parton, are utilized in the study of low transverse momentum semi-inclusive DIS (SIDIS) process and Drell-Yan process within the TMD factorization theorem. GPDs, which incorporate the transverse position information of the parton, are applied in the description of some exclusive hadronic scattering processes, such as the deeply virtual Compton scattering (DVCS) process and the deeply virtual meson production (DVMP) process. More complete one parton distribution information in the nucleon is described by Wigner distributions, or with a Fourier transform by generalized transverse momentum dependent parton distributions (GTMDs), and some theoretical explorations have been performed.

The spin structure of the nucleon has received great interests from both theoretical and experimental aspects since the discovery that the quark spin only contributes a small fraction [4, 5], about 30% in recent analyses [6, 7], to the nucleon spin. The remaining nucleon spin could be attributed to the orbital angular momenta and the gluon spin. Experimentally, many efforts have been made to measure the quark helicity term, and the gluon helicity term has also started being known in recent years [8]. In order to have a full understanding of the nucleon spin structure, one must have access to the orbital terms which are almost unknown up to now. Hence, three-dimensional images, via TMDs or GPDs, of the partonic structure in a nucleon are required. SIDIS is one of the main processes to extract TMDs.

Within the TMD factorization, SIDIS structure functions are expressed as convolutions of transverse momentum dependent parton distribution functions (TMD PDFs) and transverse momentum dependent fragmentation functions (TMD FFs). As illustrated in Figure 1, there are eight leading-twist (twist-two) quark TMD PDFs for a nucleon. If the transverse momentum is integrated, three of them (the black


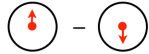
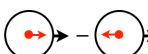

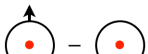
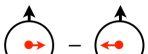
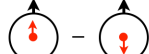
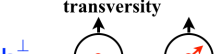
		Quark Polarization		
		U	L	T
Nucleon Polarization	U	$f_1$  unpolarized		$h_1^\perp$  Boer-Mulders
	L		$g_{1L}$  helicity	$h_{1L}^\perp$  longi-transversity (worm-gear)
	T	$f_{1T}^\perp$  Sivers	$g_{1T}$  trans-helicity (worm-gear)	$h_1$  transversity  $h_{1T}^\perp$  pretzelosity

Figure 1: Leading twist quark TMDs in a nucleon. U, L, and T denote respectively the unpolarized, longitudinal polarized, and transversely polarized configurations.

ones in Figure 1),  $f_1$ ,  $g_{1L}$ , and  $h_1$ , will reduce to their collinear limits: the unpolarized PDF, helicity distribution, and transversity distribution, while the remaining five will vanish. Hence TMDs, especially the spin-dependent ones, contain much richer information than collinear PDFs, and allow us to access the correlation between quark transverse momentum and quark/nucleon spin. The Sivers function  $f_{1T}^\perp$  and the Boer-Mulders function  $h_1^\perp$  (the red ones in Figure 1) are naively time-reversal odd TMDs, which were believed vanishing for a long time because of the time-reversal invariance property of QCD [9]. However, a model calculation indicates that nonvanishing Sivers function and Boer-Mulders function can arise from the final or initial state interactions between the struck quark and the target remnant in SIDIS or Drell-Yan process at the leading twist level [10, 11]. It was later proved that a path-order Wilson line is required in the definition of TMDs to ensure the gauge invariance [12], and it provides nontrivial phases which lead to the so-called time-reversal odd TMDs. It is a QCD version of the Aharonov-Bohm effect. In SIDIS, the Sivers function by convoluting with the unpolarized fragmentation function has leading twist contribution to a target transverse single spin asymmetry, which is referred to as the Sivers asymmetry [13]. The measurement of this asymmetry is one of the main approaches to access the Sivers function. Due to the presence of the Wilson line, opposite signs are predicted for the Sivers function as well as the Boer-Mulders function in SIDIS and Drell-Yan processes [12]. Therefore a precise measurement of the Sivers function (and the Boer-Mulders function) in both SIDIS and Drell-Yan processes is a powerful test of the QCD factorization theorem.

The transversity distribution  $h_1$  has both collinear and TMD definitions. As a probability interpretation, it represents the transversely polarized quark density in a transversely polarized nucleon. It can be viewed as the transverse counterpart to the helicity distribution that describes the longitudinally polarized quark density in a longitudinally polarized nucleon, but they are different in relativistic dynamics. The quark transversity distribution is a chiral odd quantity which does not mix with gluons but decouples from the inclusive DIS at the leading twist. In SIDIS, the transversity distribution can be measured from a target transverse single spin asymmetry, referred to as the Collins asymmetry [9], which arises from the convolution between the transversity distribution and the Collins fragmentation function.

The tensor charge, which is defined via the matrix element of a tensor current, equals to the integral of

107 the transversity distribution in the parton model. It is a fundamental QCD quantity of the nucleon, and a  
 108 precise measurement of the tensor charge is not only important for understanding the strong interaction but  
 109 also for the search of new physics beyond the standard model [14].

110 The pretzelosity distribution is another chiral odd twist-two TMD. In the wave function representation, it  
 111 is the overlap of wave functions that differ by two units of orbital angular momentum (OAM),  $|\Delta L| = 2$  [15],  
 112 and thus provides an access to quark OAM which plays a significant role in understanding the nucleon  
 113 spin structure. If neglecting the  $|L| > 1$  components of the nucleon, the pretzelosity distribution can only  
 114 originate from the overlap between  $L = 1$  and  $L = -1$  wave functions, and a more explicit relation between  
 115 the pretzelosity and quark OAM can be derived as has been given in some models [16–18]. In SIDIS, the  
 116 pretzelosity distribution can be measured from a target transverse single spin asymmetry, referred to as  
 117 the pretzelosity asymmetry, which arises from the convolution between the pretzelosity distribution and the  
 118 Collins fragmentation function at the leading twist.

## 119 1.2 TMDs in Kaon SIDIS Production

120 The Sivers asymmetry, Collins asymmetry, and pretzelosity asymmetry are also core measurements in the  
 121 approved pion SIDIS experiments [19, 20] on SoLID, as well as in other experiments [21, 22]. However, only  
 122 pion SIDIS measurements with both proton and neutron ( $^3\text{He}$ ) targets are not enough for us to have all light  
 123 flavor separations. Assuming TMD factorization, the total SIDIS cross section is a charge weighted sum of  
 124 the contributions from all flavors. Since the distribution function of the valence flavor is greater than that  
 125 of the sea and the favored fragmentation function is greater than the unfavored fragmentation function, one  
 126 will expect the main contribution is from the convolution between a valence flavor distribution function and  
 127 a favored fragmentation function.

128 As  $K^+$  contains a valence  $\bar{s}$  quark and  $K^-$  contains a valence  $s$  quark, in kaon SIDIS productions the  
 129 strange/antistrange quark is convoluted with a favored fragmentation function, and especially for  $K^-$  the  
 130 two favored fragmentations ( $s$  and  $\bar{u}$ ) are both convoluted to sea quark distributions in the nucleon. Together  
 131 with the approved pion SIDIS experiments [19, 20] on proton and  $^3\text{He}$  (neutron) targets, the measurements  
 132 of charged kaon SIDIS productions from the proton and  $^3\text{He}$  (neutron) targets will allow us to separate  
 133 contributions from all light flavors:  $u$ ,  $d$ ,  $s$ ,  $\bar{u}$ ,  $\bar{d}$ , and  $\bar{s}$ .

134 Explorations on kaon SIDIS from transversely polarized targets have been performed by HERMES [23],  
 135 COMPASS [24], and JLab Hall A collaborations [26]. As a natural expectation, one may expect the sea quark  
 136 polarization is much smaller than the valence quark polarization, which is indeed the case in the extraction  
 137 of collinear helicity distributions. However, as shown in Figures 2, 3, and 4, the single spin asymmetries of  
 138 the kaon SIDIS measured by HERMES, COMPASS, and JLab Hall A are comparable (or even larger) in size  
 139 with the asymmetries of the pion SIDIS, which contradicts with our naive expectations. Therefore, a more  
 140 precise measurement will help to clarify this issue and further improve our understanding of the nucleon spin  
 141 structure, especially the contributions from each flavor.

142 The kaon SIDIS is also proposed to be measured in some planned JLab-12 experiments with SBS using  
 143 a transverse polarized  $^3\text{He}$  target [21] and with CLAS12 using a transversely polarized HD-Ice target [22].  
 144 However, similar to the pion SIDIS case, kaon SIDIS with SoLID will have higher statistics and a complemen-  
 145 tary kinematic coverage as well as some overlap region. Furthermore, measuring the pion and kaon SIDIS  
 146 from both proton and neutron ( $^3\text{He}$ ) targets with the same Detector setup covering the same kinematic

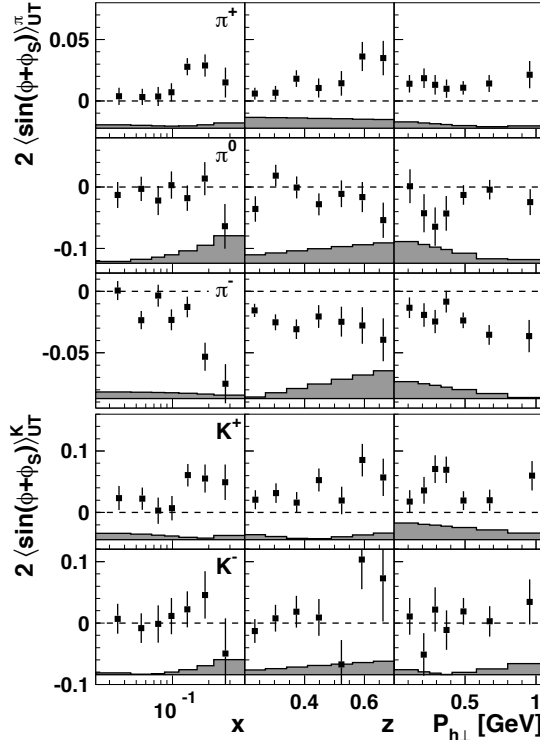


Figure 2: Collins asymmetry of pion and kaon SIDIS measured by HERMES using a transversely polarized proton target. The figure is from Ref. [23].

147 region is very important to have a direct comparison between the pion and kaon SIDIS data, perform flavor  
 148 separation of multiple quark TMDs and isolate the sea-quark contributions from the valance quarks'. To-  
 149 gether with other 12 GeV kaon SIDIS experiments, our new measurement will provide high quality data for  
 150 the continuous theoretical development of the TMD physics, and more importantly, provide strong guidance  
 151 to future measurements on electron-ion collider (EIC), which will fully study the TMD of sea quarks and  
 152 gluons in a wider kinematic coverage and provide a more complete image of nucleon structures.

In addition to strong interaction dynamics, an extraction of the strange quark tensor charge through the Collins asymmetry measurement in kaon SIDIS as mentioned above is useful in new physics explorations. For example, a permanent electric dipole moment (EDM) of any particle with a nondegenerate ground state violates both parity and time-reversal symmetries. Assuming CPT invariance, a consequence of local quantum field theories with Lorentz invariance, it is a signal of CP violation. As the Cabibbo-Kobayashi-Maskawa (CKM) complex phase requires the participation of three fermion generations, the EDM of light quarks is highly suppressed by the flavor changing interactions at the three-loop level, and thus the KM mechanism only results in an extremely small EDM. Hence, the quark EDM is one of the most sensitive probes to new physics beyond the SM. Since quarks are confined in hadron, one has to access quark EDMs via nucleon EDM measurements, and the tensor charge serves as the weighting factor,

$$d_N = \sum_q g_T^q d_q, \quad (1)$$

153 where  $g_T^q$  is the tensor charge of flavor- $q$ ,  $d_q$  is the EDM of flavor- $q$ , and  $d_N$  is the nucleon EDM. Up to now,

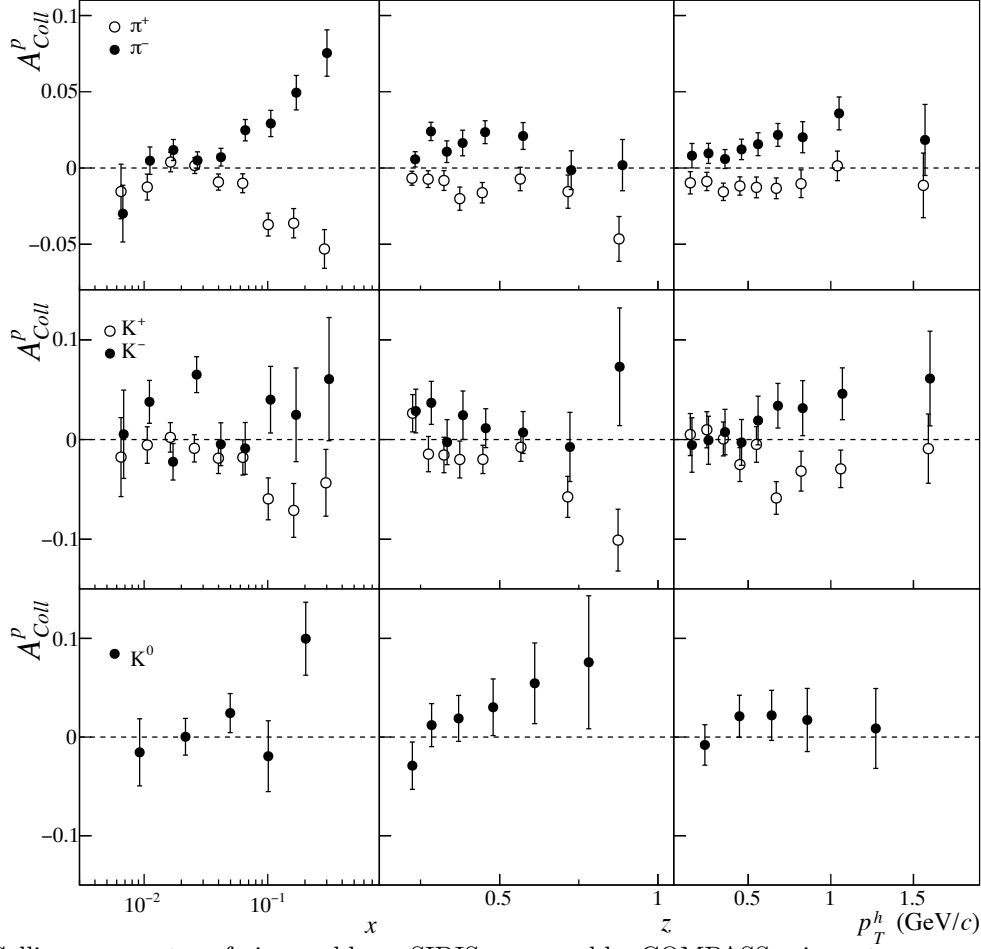


Figure 3: Collins asymmetry of pion and kaon SIDIS measured by COMPASS using a transversely polarized proton target. The figure is from Ref. [24].

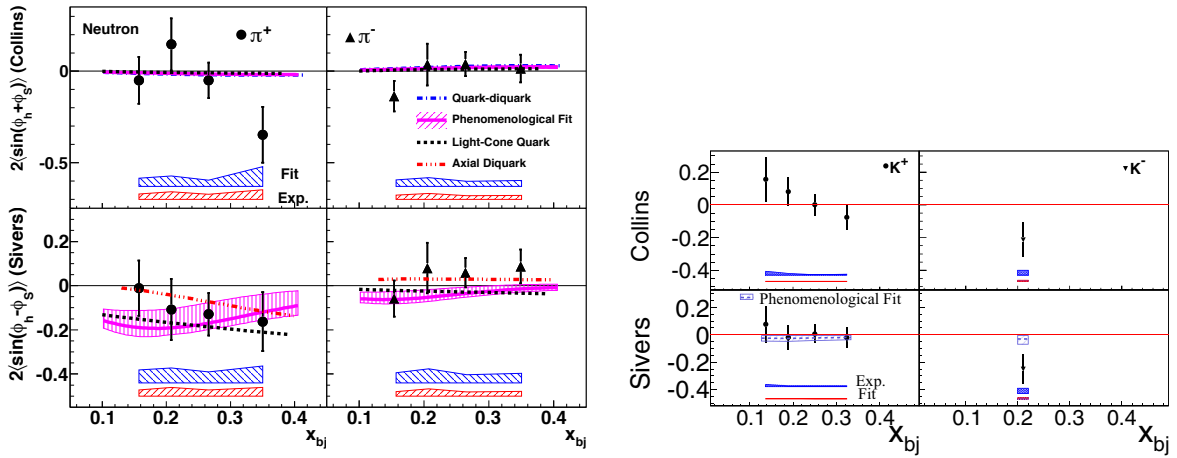


Figure 4: Collins and Sivers asymmetries of pion and kaon SIDIS measured by JLab Hall A using a transversely polarized  $^3\text{He}$  target. The figures are from Refs. [25, 26].



154 all global analysis of transversity distributions and thus tensor charge extractions assume zero strangeness  
 155 contribution due to the limited precision of the data. On the other hand, the strange quark EDM is expected  
 156 to be much larger than that of the down quark in most new physics models, because the quark EDM is roughly  
 157 proportional to the quark mass based on a simple dimensional analysis following the effective field theory.  
 158 Therefore the extraction of the strange quark tensor charge is important in quantifying the strange quark  
 159 EDM contribution to the nucleon EDM and then testing new physics models.

### 160 1.3 Spin asymmetries in SIDIS

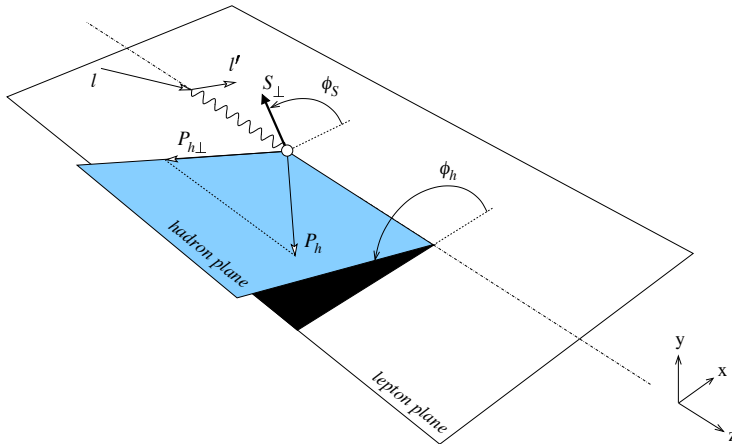


Figure 5: Definitions of azimuthal angles and the transverse momentum of the detected hadron in SIDIS process. They follow the Trento convention [27]. The figure is taken from Ref. [28].

In the semi-inclusive deep inelastic scattering, the lepton is scattered off the nucleon, and one of the hadrons produced in the collision is detected in coincidence with the scattered lepton. The process is expressed as

$$e(l) + N(P) \rightarrow e(l') + h(P_h) + X(P_X), \quad (2)$$

where the lepton in the reaction is set as electrons ( $e$ ),  $N$  is the nucleon,  $h$  is the detected hadron, and  $X$  represents undetected particles. Four momenta of them are given in parentheses. As usual, the kinematics are expressed in terms of Lorentz scalar variables,

$$Q^2 = -q^2 = -(l - l')^2, \quad x = \frac{Q^2}{2P \cdot q}, \quad z = \frac{P \cdot P_h}{P \cdot q}, \quad (3)$$

161 where  $q$  is the transferred four-momentum, and with one-photon exchange approximation it is the four-  
 162 momentum of the virtual photon. As illustrated in Figure 5, azimuthal angles and the transverse momentum  
 163 of the hadron are defined following the Trento convention [27]. The hadron transverse momentum  $\mathbf{P}_{h\perp}$   
 164 is defined in the photon-nucleon collinear frame,  $\phi_h$  is the azimuthal angle from the lepton plane to the hadron  
 165 plane, and  $\phi_S$  is the azimuthal angle from lepton plane to the nucleon polarization direction if it is transversely  
 166 polarized.

Assuming one-photon exchange, the differential cross section of SIDIS can be expressed in terms of 18

structure functions according to different beam and target polarizations and azimuthal modulations,

$$\begin{aligned}
\frac{d\sigma}{dx dy dz d\psi d\phi_h d\mathbf{P}_{h\perp}^2} &= \frac{\alpha^2}{xyQ^2} \frac{y^2}{2(1-\epsilon)} \left(1 + \frac{\gamma^2}{2x}\right) \left\{ F_{UU,T} + \epsilon F_{UU,L} + \sqrt{2\epsilon(1+\epsilon)} \cos\phi_h F_{UU}^{\cos\phi_h} \right. \\
&\quad + \epsilon \cos 2\phi_h F_{UU}^{\cos 2\phi_h} + \lambda_e \sqrt{2\epsilon(1-\epsilon)} \sin\phi_h F_{LU}^{\sin\phi_h} \\
&\quad + S_L \left[ \sqrt{2\epsilon(1+\epsilon)} \sin\phi_h F_{UL}^{\sin\phi_h} + \epsilon \sin 2\phi_h F_{UL}^{\sin 2\phi_h} \right] \\
&\quad + S_L \lambda_e \left[ \sqrt{1-\epsilon^2} F_{LL} + \sqrt{2\epsilon(1-\epsilon)} \cos\phi_h F_{LL}^{\cos\phi_h} \right] \\
&\quad + S_T \left[ \sin(\phi_h - \phi_S) (F_{UT,T}^{\sin(\phi_h - \phi_S)} + \epsilon F_{UT,L}^{\sin(\phi_h - \phi_S)}) \right. \\
&\quad + \epsilon \sin(\phi_h + \phi_S) F_{UT}^{\sin(\phi_h + \phi_S)} + \epsilon \sin(3\phi_h - \phi_S) F_{UT}^{\sin(3\phi_h - \phi_S)} \\
&\quad \left. + \sqrt{2\epsilon(1+\epsilon)} \sin\phi_S F_{UT}^{\sin\phi_S} \sqrt{2\epsilon(1+\epsilon)} \sin(2\phi_h - \phi_S) F_{UT}^{\sin(2\phi_h - \phi_S)} \right] \\
&\quad + S_T \lambda_e \left[ \sqrt{1-\epsilon^2} \cos(\phi_h - \phi_S) F_{LT}^{\cos(\phi_h - \phi_S)} + \sqrt{2\epsilon(1-\epsilon)} \cos\phi_S F_{LT}^{\cos\phi_S} \right. \\
&\quad \left. + \sqrt{2\epsilon(1-\epsilon)} \cos(2\phi_h - \phi_S) F_{LT}^{\cos(2\phi_h - \phi_S)} \right] \left. \right\}, \tag{4}
\end{aligned}$$

where  $\alpha$  is the electromagnetic fine structure constant,  $\lambda_e$  denotes the lepton beam helicity,  $S_L$  and  $S_T$  are target longitudinal and transverse polarizations, and the structure functions  $F$  are four dimensional functions of  $x$ ,  $Q^2$ ,  $z$ , and  $\mathbf{P}_{h\perp}^2$ . The angle  $\psi$  is the azimuthal angle of the scattered lepton around the lepton beam axis with respect to a fixed direction. The exact relation between  $\psi$  and  $\phi_S$  is derived in Ref. [29]. In the deep inelastic kinematics, one has  $d\psi \approx d\phi_S$ . The subscripts of the structure functions indicate the beam and target polarizations, and the third subscript specifies the virtual photon polarization. The  $\epsilon$  is the ratio of longitudinal and transverse photon flux,

$$\epsilon = \frac{1 - y - \frac{1}{4}\gamma^2 y^2}{1 - y + \frac{1}{2}y^2 + \frac{1}{4}\gamma^2 y^2}, \tag{5}$$

167 where  $\gamma = 2Mx/Q$  and  $M$  is the nucleon mass.

Integration over the azimuthal angles, the cross section is expressed as

$$\frac{d\sigma}{dx dy dz d\mathbf{P}_{h\perp}^2} = \frac{4\pi^2 \alpha^2}{xyQ^2} \frac{y^2}{2(1-\epsilon)} \left(1 + \frac{\gamma^2}{2x}\right) F_{UU}(x, Q^2, z, \mathbf{P}_{h\perp}^2) = 4\pi^2 \sigma_0. \tag{6}$$

For a unpolarized beam scattered off a transversely polarized target, one can define the asymmetries,

$$\begin{aligned}
\frac{d\sigma}{dx dy dz d\mathbf{P}_{h\perp}^2 d\phi_h d\phi_S} &= \sigma_0 \left\{ 1 + \cos\phi_h A_{UU}^{\cos\phi_h} + \cos 2\phi_h A_{UU}^{\cos 2\phi_h} \right. \\
&\quad + S_T \left[ \sin(\phi_h - \phi_S) A_{UT}^{\sin(\phi_h - \phi_S)} + \sin(\phi_h + \phi_S) A_{UT}^{\sin(\phi_h + \phi_S)} \right. \\
&\quad \left. + \sin(3\phi_h - \phi_S) A_{UT}^{\sin(3\phi_h - \phi_S)} + \sin\phi_S A_{UT}^{\sin\phi_S} + \sin(2\phi_h - \phi_S) A_{UT}^{\sin(2\phi_h - \phi_S)} \right] \left. \right\}, \tag{7}
\end{aligned}$$

where

$$A_{UU}^{\cos \phi_h} = \frac{\sqrt{2\varepsilon(1+\varepsilon)}F_{UU}^{\cos \phi_h}}{F_{UU}}, \quad (8)$$

$$A_{UU}^{\cos 2\phi_h} = \frac{\varepsilon F_{UU}^{\cos 2\phi_h}}{F_{UU}}, \quad (9)$$

are unpolarized azimuthal modulations, and

$$A_{UT}^{\sin(\phi_h-\phi_s)} = \frac{F_{UT}^{\sin(\phi_h-\phi_s)}}{F_{UU}}, \quad (10)$$

$$A_{UT}^{\sin(\phi_h+\phi_s)} = \frac{\varepsilon F_{UT}^{\sin(\phi_h+\phi_s)}}{F_{UU}}, \quad (11)$$

$$A_{UT}^{\sin(3\phi_h-\phi_s)} = \frac{\varepsilon F_{UT}^{\sin(3\phi_h-\phi_s)}}{F_{UU}}, \quad (12)$$

$$A_{UT}^{\sin \phi_s} = \frac{\sqrt{2\varepsilon(1+\varepsilon)}F_{UT}^{\sin \phi_s}}{F_{UU}}, \quad (13)$$

$$A_{UT}^{\sin(2\phi_h-\phi_s)} = \frac{\sqrt{2\varepsilon(1+\varepsilon)}F_{UT}^{\sin \phi_s}}{F_{UU}}, \quad (14)$$

$$(15)$$

168 are target transverse single spin asymmetries.

169 Assuming TMD factorization, one has three target transverse spin asymmetries at the leading twist  
 170 level:  $A_{UT}^{\sin(\phi_h-\phi_s)}$ ,  $A_{UT}^{\sin(\phi_h+\phi_s)}$ , and  $A_{UT}^{\sin(3\phi_h-\phi_s)}$ . They respectively correspond to the Sivers, Collins, and  
 171 pretzelocity asymmetries, which as discussed above are proportional to the convolutions  $f_{1T}^\perp \otimes D_1$ ,  $h_1 \otimes H_1^\perp$ ,  
 172 and  $h_{1T}^\perp \otimes H_1^\perp$  at the leading twist. Here  $D_1$  is the unpolarized fragmentation function and  $H_1^\perp$  is the Collins  
 173 fragmentation function.

## 174 1.4 SIDIS kinematic regions

175 As discussed above, the TMD factorization is the underlying theorem that allows us to extract TMDs  
 176 from SIDIS measurements, but the factorization is only valid for certain kinematic regions. For the photon  
 177 virtuality to be acceptable as a hard scale,  $Q^2 \gg \Lambda_{\text{QCD}}^2$  must be satisfied. In this proposal, we require  
 178  $Q^2 > 1 \text{ GeV}^2$ . When the detected hadron transverse momentum  $\mathbf{P}_{h\perp}$  is large, it is associated with the  
 179 transverse momentum generated from hard radiations, and then one can apply the collinear factorization.  
 180 For the kinematic coverage by SoLID detector, we are measuring the SIDIS process with small  $\mathbf{P}_{h\perp}$ . As  
 181 illustrated in Figure 6, one can define three regions: (a) current fragmentation, (b) target fragmentation,  
 182 and (c) central (or soft) regions [30].

183 **Current fragmentation region:** the outgoing struck quark fragments into the detected hadron, which  
 184 continues moving roughly in the same direction with roughly the same rapidity. It has a fully developed  
 185 TMD factorization treatment. The structure functions can be expressed in terms of TMD PDFs and TMD  
 186 FFs. This region has received the most theoretical attention and is also the region we can extract the Sivers  
 187 function, the transversity distribution, and the pretzelocity distribution discussed above.

188 **Target fragmentation region:** the detected hadron is generated from the remnant of the nucleon, and  
 189 its momentum is roughly collinear to the target. It is described in terms of extended fracture functions.

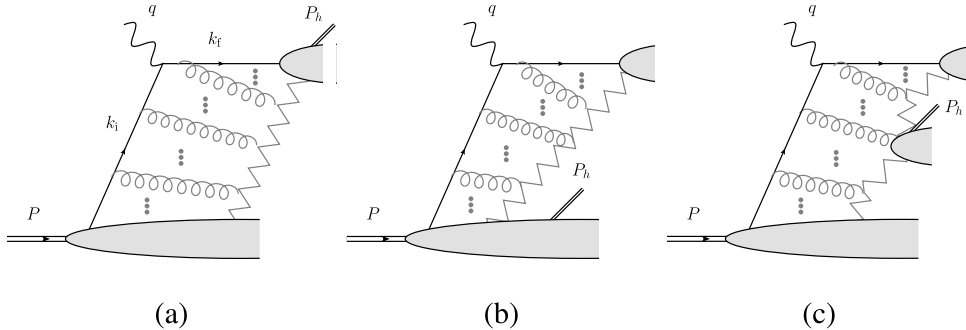


Figure 6: Kinematic regions of SIDIS at small  $\mathbf{P}_{h\perp}$ . (a) The current fragmentation region; (b) the target fragmentation region; (c) the central (soft) region. The figure is from Ref. [30].

190 **Central (or soft) fragmentation region:** the produced hadron's rapidity is much less than that of  
 191 the target but much greater than that of the outgoing quark (or current jet). A factorization theorem for  
 192 the central fragmentation region is in principle possible but has not been worked out yet.

193 An important point is that the classification of the three regions is not sharp. They overlap with each  
 194 other, and the real SIDIS process is a mix of them. But at certain kinematics, one can identify one of them  
 195 dominates the process. Once factorization theorems are developed for all three regions, one can match the  
 196 factorization from one region to another region to have a unified description.

Although one cannot clearly separate the three regions, a ratio factor

$$R_1 = \frac{P_h \cdot k_f}{P_h \cdot k_i} \quad (16)$$

197 is defined by theorists as criteria to identify which region is the dominant one for a given SIDIS process [30,31].  
 198 Here  $k_f$  and  $k_i$  are the four-momenta of the outgoing quark and the incoming quark as labeled in Figure 6.  
 199 When  $R_1$  is small, one can identify the process in the current fragmentation region, because in this case the  
 200 hadron momentum  $P_h$  is roughly parallel to the outgoing quark and thus the numerator  $P_h \cdot k_f$  is small.  
 201 When  $R_1$  is large, *i.e.*  $1/R_1$  is small, one can identify the process in the target fragmentation region, because  
 202 in this case the hadron momentum  $P_h$  is roughly parallel to the target as well as the incoming quark and  
 203 thus the denominator  $P_h \cdot k_i$  is small. When  $R_1 \sim 1$ , one can identify it in the central region.

204 To estimate the value of  $R_1$ , one has to make some assumptions. Here we follow the procedure in Ref. [31]  
 205 and perform a Monte Carlo sampling with SoLID kinematics. In Figure 7, we show the  $R_1$  distributions of  
 206 SoLID kaon SIDIS events. Kinematic cuts:  $Q^2 > 1 \text{ GeV}^2$ ,  $W > 2.3 \text{ GeV}$ ,  $W' > 1.6 \text{ GeV}$ , and  $0.3 < z < 0.7$   
 207 have been applied. Using  $R_1 < 0.4$  and  $1/R_1 < 0.4$  to separate the current fragmentation region and the  
 208 target fragmentation region from the full range, we will have about 20% events in the current fragmentation  
 209 region and about 10% events in the target fragmentation region.

210 The kaon SIDIS events in the current fragmentation region can be used to extracted quark Sivers,  
 211 transversity, pretzelocity and other TMDs. A wide coverage from the current fragmentation region to the  
 212 central region and even to the target fragmentation region will help to learn the transition from one region  
 213 to another region and to estimate the corrections in the TMD extractions using the data in the current  
 214 fragmentation region. Combining the data that will be collected here at low- $Q^2$  and future EIC data at  
 215 high- $Q^2$ , one will have a wide kinematic range, which is important in quantifying the correction terms.

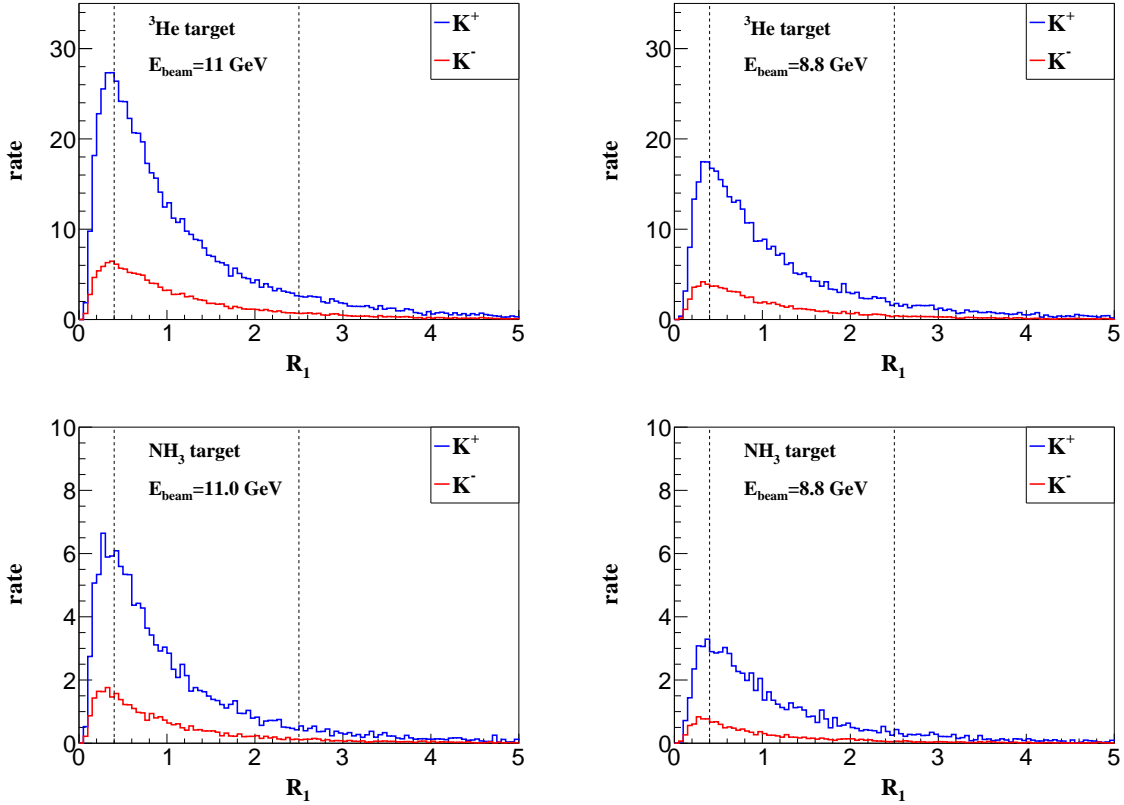


Figure 7: SoLID kaon SIDIS kinematic regions ( $R_1$  distributions). The left panel is with 11 GeV beam, and the right panel is with 8.8 GeV beam. The blue curves are  $R_1$  distributions for  $K^+$ -SIDIS, and the red curves are those for  $K^-$ -SIDIS. Kinematics cuts:  $Q^2 > 1 \text{ GeV}^2$ ,  $W > 2.3 \text{ GeV}$ ,  $W' > 1.6 \text{ GeV}$ , and  $0.3 < z < 0.7$ , have been applied. The vertical dashed lines correspond to  $R_1 = 0.4$  and  $R_1^{-1} = 0.4$ . From left (small  $R_1$ ) to right (large  $R_1$ ), it transits from the current fragmentation region to the central fragmentation region and finally to the target fragmentation region.

## 2 Experimental Setup

We propose to measure the  $K^\pm$  production in the Semi-Inclusive Deep-Inelastic Scattering (SIDIS) with both polarized proton and neutron targets by using Solenoidal Large Intensity Device (SoLID) [32]. It will be a natural extension of the already approved SIDIS experiments on SoLID to measure  $\pi^\pm$  production with polarized neutron target (E12-10-006 [19], E12-11-007 [33]) and with the polarized proton target (E12-11-108 [20]).

SoLID has two configurations of the detector system, called SoLID-SIDIS and SoLID-PVDIS. Besides E12-10-006, two SIDIS experiments, E12-11-007 [33] and E12-11-108 [20], along with the  $J/\psi$  experiment (E12-12-006 [34]), will also use the SoLID-SIDIS configuration. All of these experiments have been approved with A or A- rating. In addition, two “bonus-run” experiments, E12-10-006A [35] and E12-11-108A [36], have also been approved to run in parallel with the SIDIS experiments. Another “bonus-run” experiment, E12-10-006B [38] was also approved to perform the measurement of deep virtual meson production (DVMP) to study GPD as with the SoLID-SIDIS setup. The SoLID-PVDIS configuration is for the Parity Violation in Deep Inelastic Scattering (PVDIS) [37].

The solenoid magnet for SoLID is based on the CLEO-II magnet built by Cornell University. The magnet has coil length of 3.5 m with an inner cryostat diameter of 2.9 m. The max field strength is about 1.4 Tesla, with an integrated BDL close to 5 Tesla-meters. The fringe field at the front end after shielding can be controlled less than 5 Gauss. In the SIDIS-configuration, the CLEO-II magnet provides  $2\pi$  acceptance in the azimuthal angle ( $\phi$ ) and covers polar angle ( $\theta$ ) from  $8^\circ$  up to  $24^\circ$ . The momentum acceptance is between 0.8 and 7.5 GeV/c for electrons and hadrons. The momentum resolution is about 2% and angle resolution is about a few mrad.

The layout of the SoLID detectors in the SIDIS-configuration is shown in Fig. 8. The detector system is divided into two regions for the forward-angle (FA) detection and the large-angle (LA) detection. Six tracking chambers based on Gas Electron Multipliers (GEM) will be used for charged particle tracking in the forward-angle region, and the first four of them will be shared by the large-angle region. In each region, a Shashlyk-type sampling EM calorimeter (LAEC or FAEC) will measure the particle energy and identify electrons from hadrons. Two scintillator-pad detectors, LASPD and FASPD, will be installed in front of each EC to reject photons and provide timing information for the large-angle. The forward-angle detectors will detect both the electrons and hadrons. A light-gas Čerenkov detector (LGC) and a heavy-gas Čerenkov detector (HGC) will perform the  $e/\pi^\pm$  and  $\pi^\pm/K^\pm$  separation, respectively. The Multi-gap Resistive Plate Chamber (MRPC) will provide a precise time measurement for the forward going charged particles and it will also provide some photon rejection.

The proposed measurement on neutron will utilize the polarized  $^3\text{He}$  target as an effective neutron target. Such a target was successfully employed in E06-110, a 6 GeV SIDIS experiment in Hall A. The polarized  $^3\text{He}$  target is based on the technique of spin-exchange optical pumping of hybrid Rb-K alkali atoms. There are two sets of Helmholtz coils with a magnetic field in the order of 25 Gauss to provide the transverse and longitudinal polarization. The  $^3\text{He}$  gas with a density of about 10 amg (10 atm at  $0^\circ$ ) is stored in a 40 cm target cell made of thin glasses. With a 15  $\mu\text{A}$  electron beam, the neutron luminosity can be as high as  $10^{36} \text{ cm}^{-2}\text{s}^{-1}$ . The in-beam polarization of 60% was archived during the E06-110 experiment. Two kinds of polarimetry, NMR and EPR, were used to measure the polarization with relative 5% precision. We have plans to improve the accuracy of the measurement to reach 3%. The proposed measurement on proton will

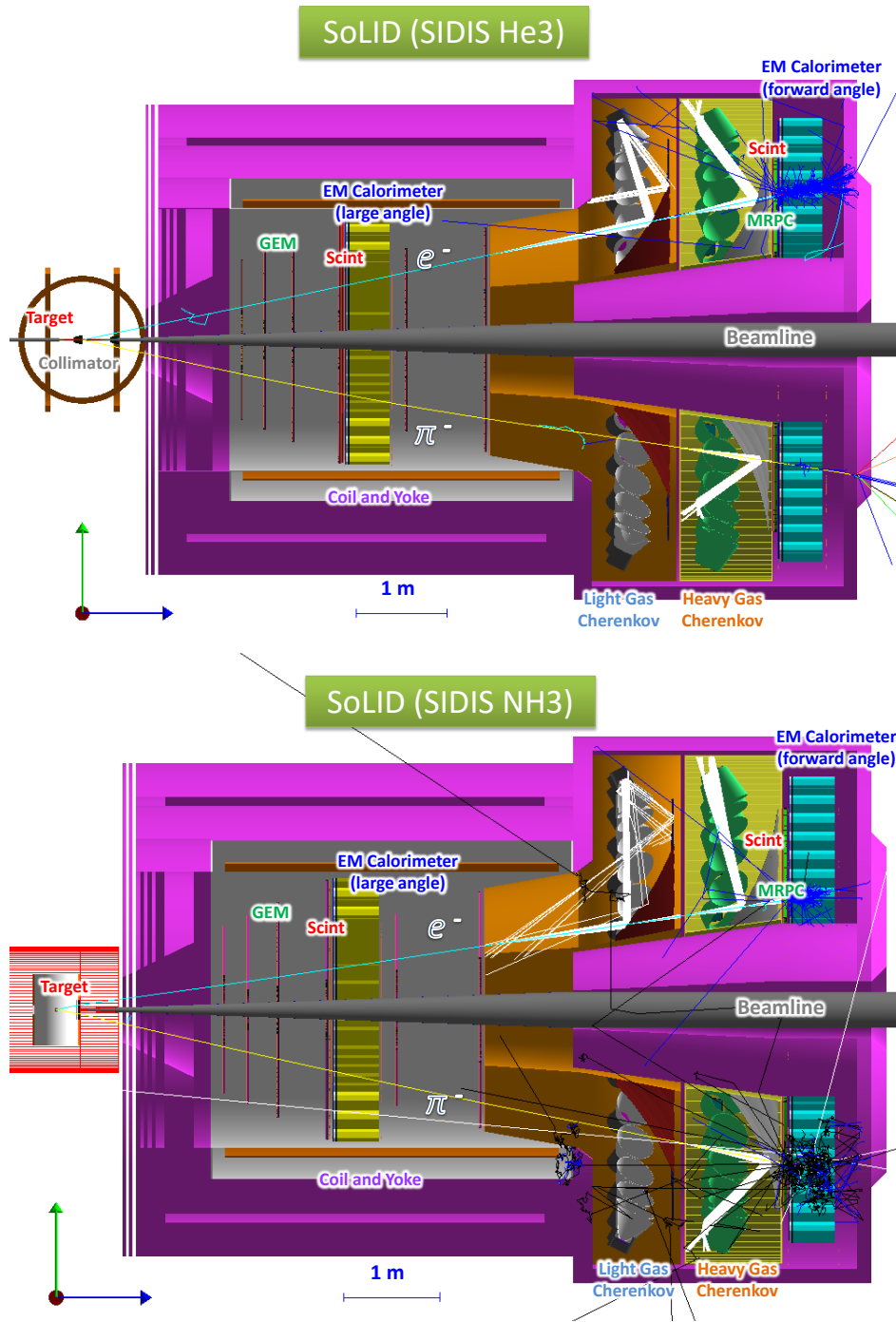


Figure 8: The Detector Layout of the SoLID-SIDIS configuration with either <sup>3</sup>He or NH<sub>3</sub> target. The detector system includes six Gas Electron Multiplier (GEM) planes for charged particle tracking, two Scintillator Pad Detectors (SPD) followed by two Shashlyk sampling EM Calorimeters (EC) for electron and photon energy measurement and particle identification, a Light Gas Čerenkov Detector (LGC) for  $e-\pi^\pm$  separation, a Heavy Gas Čerenkov Detector (HGC) for  $\pi^\pm-K^\pm$  separation, as well as a Multi-gap Resistive Plate Chamber (MRPC) for time measurement. The 1 - 4 GEM trackers, the large-angle SPD (LASPD) and large-angle EC (LAEC) form the large-angle detection system for electron measurement. The forward-angle detection system, to measure electron and hadrons, is composed of all 2-6 GEM trackers, LGC, HGC, MRPC, the forward-angle SPD (FASPD) and the forward-angle EC (FAEC). The polarized <sup>3</sup>He target is shown with both longitudinal and transverse field coils. The transversely polarized NH<sub>3</sub> target is shown with its solenoid field and scattering chamber.

257 use the dynamically polarized ammonia target. It has been used at SLAC and at Jefferson on numerous  
 258 occasions. Its last use as a longitudinally polarized target was in 2012 for the g2p/Gep experiments, which  
 259 took place in Hall A. Proton luminosities of  $10^{35} \text{ cm}^{-2}\text{s}^{-1}$  with 90% polarization have been achieved with  
 260 this target, in conjunction with electron beam currents up to 100 nA. For the SoLID measurement, a new  
 261 5T magnet will be constructed to make it a transversely polarized target.

262 A more detailed discussion of the design, simulation, prototype-test of each detector and targets is given  
 263 in the SoLID preliminary conceptual design report (pCDR) [32].

264 **As a run group proposal, this new measurement has no requirement of extra beam-time**  
 265 **or configuration change. The existing detector systems like the HGC and the MRPC already**  
 266 **can identify kaons from other charged particles at certain momentum limits. However, to**  
 267 **cleanly detect large-momentum kaons this experiment does require an improvement on the**  
 268 **time resolution of the time-of-flight (TOF) detector. The MRPC will need to improve its time**  
 269 **resolution down to 20 ps so that we can use the TOF information to sufficiently separate kaons**  
 270 **from pions up to 7 GeV/c. In the next section, we will demonstrate that such a new requirement will**  
 271 **be achievable with current technologies.**

## 272 3 Kaon Identification

### 273 3.1 Overview

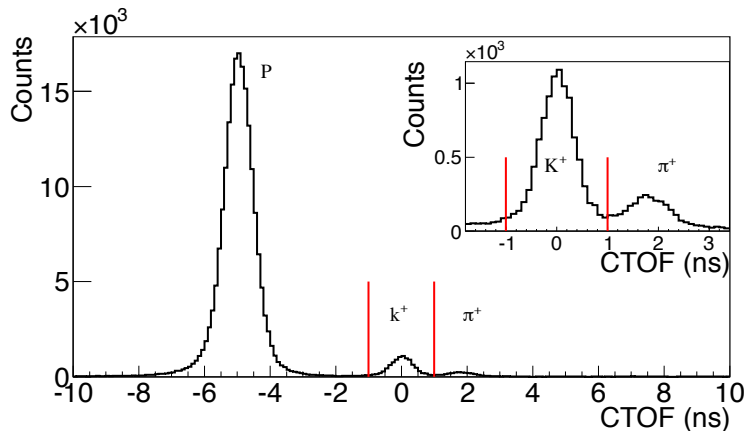


Figure 9: Hall A 6 GeV Transversity experiment coincidence timing spectrum after a cut on the aerogel detector to remove  $\pi^\pm$ .

274 The kaon identification at the forward-angle will be performed by using the Heavy Gas Čerenkov (HGC)  
 275 detector and the high-resolution time-of-flight (TOF) information from the MRPC detector. The HGC  
 276 detector will separate  $K^\pm$  from  $\pi^\pm$  in the momentum range from 2.2 GeV/c to 7.0 GeV/c by vetoing the  
 277 HGC signals during the offline event selection. With reasonable time resolution (e.g. 80 ps), the MRPC's  
 278 TOF can easily isolate  $K^\pm$  from protons up to 6 GeV/c and from  $\pi^\pm$  at low momenta ( $<3.5$  GeV/c). A  
 279 50 ps time resolution can reject protons in the full momentum range. With 20 ps time resolution, the MRPC  
 280 can also distinguish  $K^\pm$  and  $\pi^\pm$  up to 7.0 GeV/c. The cross-reference of these two detector systems will  
 281 also allow us to optimize the PID cuts and evaluate the PID efficiencies. Combining these two detectors we



282 will effectively detect  $K^\pm$  with good efficiency and small pion contamination. A similar method has been  
 283 proved to be very effective from the Hall A 6 GeV Transversity experiment which used an aerogel Čerenkov  
 284 detector and scintillator counters for TOF [26].

### 285 3.2 Pion rejection by HGC Detector

286 The HGC uses  $C_4F_8O/C_4F_{10}$  gas at a pressure of 1.5 atm and a temperature of 20 °C as the radiator. It  
 287 works as a threshold detector where the threshold is roughly 2.2 GeV for  $\pi^\pm$  and 7 GeV for  $K^\pm$ . The gas  
 288 length available for Čerenkov light production is about 1 m due to geometrical acceptance constraints and it  
 289 covers the entire polar angles in the forward-angle region with a full azimuthal coverage. The optical system  
 290 consists of a ring of 30 spherical mirrors and light reflection cones around PMT assemblies. Each mirror will  
 291 have a PMT assembly made of 16 Hamamatsu Multi-anode PMTs (H12700) as photon detectors.

292 The HGC's primary goal would be to provide pion identification with kaon suppression and it relies on  
 293 placing cuts on the collected number of photoelectrons above the average background level. If we set the  
 294 threshold reasonably high, we can use the HGC as a veto detector to reject most of  $\pi^\pm$  and thus help kaon  
 295 identification together with the MRPC's TOF information.

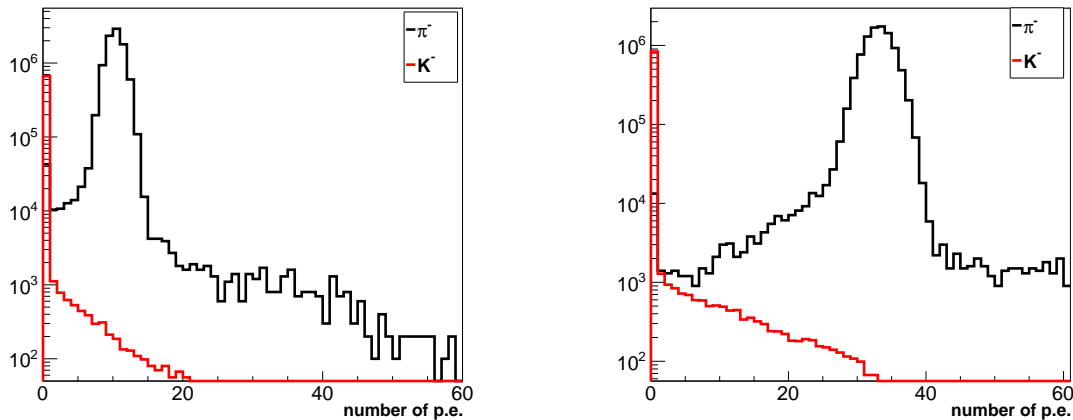


Figure 10: The number of photoelectrons of  $\pi^\pm$  and  $K^\pm$  in HGC from 8 deg polar angle at 2.5 GeV (left) and 7 GeV (right) momentum.

296 We have performed a simplified simulation with the HGC to demonstrate the feasibility. We simulated  
 297 both negative pion and kaon response of HGC as a part of the whole SoLID-SIDIS  $^3\text{He}$  setup. The number  
 298 of  $\pi^\pm$  is assumed to be 10 times the number of  $K^\pm$ . Our simulation only uses  $\pi^\pm$  and  $K^\pm$  emitted from the  
 299 target center and at a polar angle of 8 deg with the momenta of 2.5 GeV and 7 GeV. The 8 deg polar angle  
 300 is selected because it has shortest radiator length, thus the lowest number of Čerenkov photons a pion will  
 301 generate and is most difficult to reject. As shown in Figure 10, the  $\pi^\pm$  and  $K^\pm$  are well separated while  
 302  $K^\pm$  show small tails with a very small number of events. This result doesn't include any noise from PMT  
 303 and DAQ system and there is no integration over a time windows. The overall efficiency of pion suppression  
 304 will need to be evaluated in a combined study of both HGC and MRPC. If we apply a conservative cut at 5  
 305 photoelectrons, we obtain a factor of 100 pion rejection at 2.5 GeV and 400 at 7 GeV.

306 **3.3 Time-Of-Flight PID**

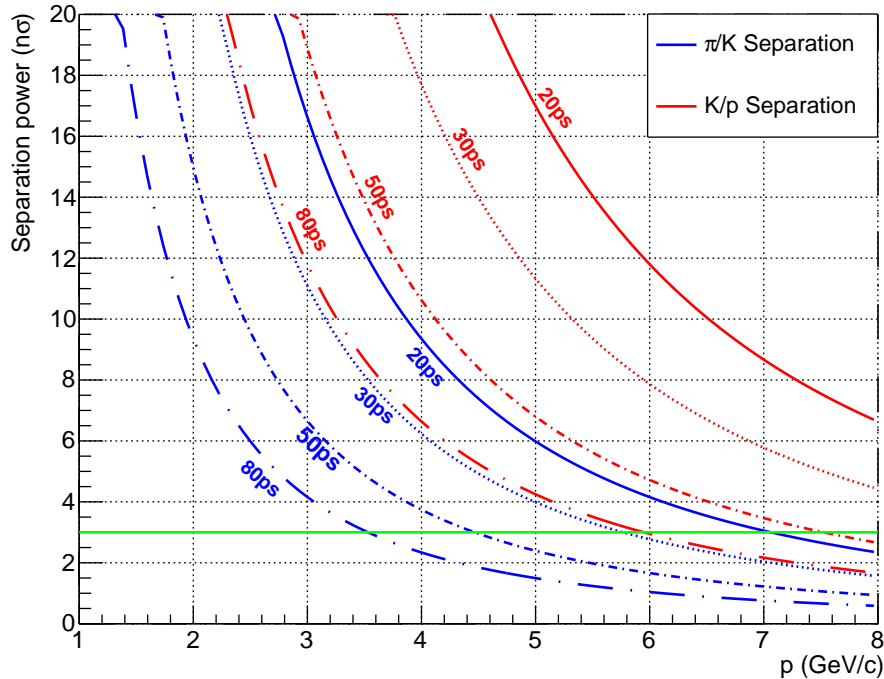


Figure 11: The separation power between  $\pi^\pm$  and  $K^\pm$  (blue) and  $K^\pm$  and protons (red) as a function of the particle momentum for different time resolutions. The total path length is around 8 m.

307 While the momenta of charged particles can be determined by reconstructing their tracks traveling in a mag-  
 308 netic spectrometer, the masses (hence the particle types) of these particles can be determined by measuring  
 309 the TOF after a fixed distance  $L$ :

$$m = \frac{p}{c} \sqrt{\frac{c^2 t^2}{L^2} - 1}. \quad (17)$$

310 Coming from the same location (such as the target), two charged particles with the same momenta but with  
 311 different masses will have different arrival times when reaching the same detector:

$$\Delta t = t_1 - t_2 \simeq \frac{Lc}{2p^2} (m_1^2 - m_2^2). \quad (18)$$

312 One can define the separation power of a TOF detector by taking the ratio of the time difference of two  
 313 particles to the time resolution of the detector:

$$n_\sigma = \Delta t / \sigma_{TOF} \quad (19)$$

314 For SoLID, the MRPC will be used as the TOF system. Figure 11 shows the separation power of the  
 315 MRPC with different time resolutions for a total flight distance of 8 m. With a time resolution of 20 ps, one  
 316 can obtain a  $3\sigma$  separation between  $\pi^\pm$  and  $K^\pm$  up to a particle momentum of 7 GeV/c. Even at the 30 ps  
 317 level, we still can identify  $K^\pm$  up to 6 GeV/c. As shown in Section 4.1, only a small amount of  $K^\pm$  have  
 318 momenta above 6 GeV/c where the HGC is expected to more efficiently separate  $\pi^\pm$  and  $K^\pm$  as discussed  
 319 in the previous section.

### 3.4 MRPC Detector

The prototype design of the SoLID MRPC is shown in Fig.12. The detector consists of 50 super-modules and each super-module has 3 MRPC modules. There is overlap between modules to avoid the blind area. In each module, there are 10 gas gaps. Each gas gap has a width of 0.25 mm and is separated by 0.7 mm thick glass layers. Tsinghua University has developed a new type of low-resistive glass with the bulky resistivity on the order of  $10 \Omega\text{cm}$ . The rate capability of this MRPC assembly, with this type of glass, can reach  $50 \text{ kHz}/\text{cm}^2$ . More details on the MRPC design can be found in the SoLID pCDR [32].

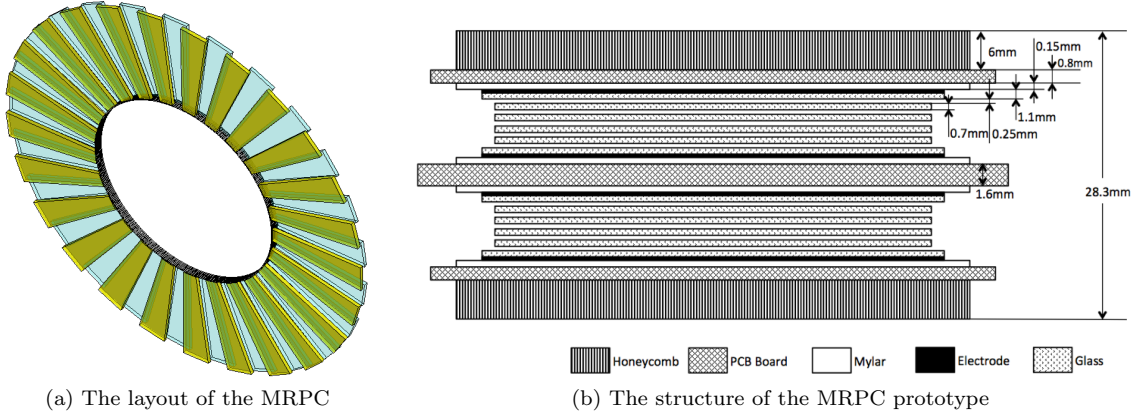


Figure 12: The MRPC prototype design.

The MRPC prototype developed by Tsinghua University has been tested with both cosmic rays and beam [39]. The cosmic test reported an efficiency over 95% and a time resolution around 50 ps with relatively slow front-end electronics. The beam test was performed at JLab utilizing the electron beam during the g2p experiment. The range of particle flux for the beam test was from 1 to  $16 \text{ kHz}/\text{cm}^2$ . A timing resolution of 80 ps and an efficiency over 94% were obtained even when the flux reached  $15 \text{ kHz}/\text{cm}^2$ .

### 3.5 Recent MRPC R&D Progresses

There are two major contributions to the time resolution: the time response of the detector and the performance of front-end electronics. While the time resolution of modern low-noise fast electronics is already very good (only a few pico-seconds), the dominant limitation is from the actual performance of the detector, particularly in a high-rate environment. The ALICE-TOF MRPC reportedly reached 57 ps in the full operation [40] and the ongoing R&D effort is to upgrade the time resolution to be less than 20 ps and also increase the rate capability for the upcoming HL-LHC running. In the last ten years, several R&D works [41, 42] have shown a 20 ps level time resolution on MRPC detectors. The most recent MRPC designed for the ALICE-TOF upgrade showed a time resolution of 16 ps [43]. In the U.S., there is an EIC R&D project (EIC RD2013-5 [44]) to apply the state-of-art time technologies to push the time resolution down to only a few ps for future large-area TOF detector systems including the the next generation MRPC detectors. A thin-gas-gap MRPC prototype developed by members of this collaboration (UIUC and BNL) provided an 18 ps time resolution with the cosmic ray ( $25 \text{ ps}$  at  $80\text{Hz}/\text{cm}^2$ ). Their ongoing R&D effort is also trying to develop a low current, high analog bandwidth preamp for use in fast timing applications.

There has been a joint R&D effort from a Chinese collaboration to develop the next generation MRPC

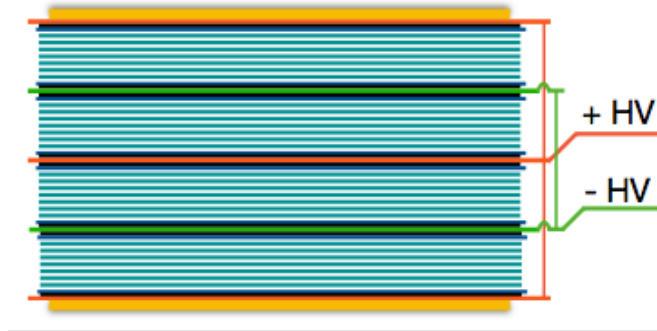


Figure 13: The structure of the testing MRPC at Tsinghua University

347 for RHIC, SoLID and EIC. In the previous MRPC generations, the signal was read out with NINOs or PADI  
 348 front-end electronics(FEE) and the time was given with TDC channels. However, the time jitter of the  
 349 TDC is usually larger than 20 ps and is not suitable for high precision time measurements. The front-end  
 350 electronics is thus planned to be a fast amplifier and a charge digitizer, in order to take the record of the  
 351 signal waveform from the MRPC detector.

352 The MRPC designed for SoLID has a thin gas gap of 104 um. There are 4 stacks with 8 gaps per stack.  
 353 A detailed simulation of this MRPC has been made and the waveforms from the FEE was obtained. A time  
 354 reconstruction method based on the neural network and machine learning algorithms has been developed to  
 355 take the full use of the information in the signal waveform [45]. The neural network is a powerful tool in  
 356 solving non-linear pattern recognition problems and has many applications in the fields of not only computer  
 357 science but also high energy physics as well. In this time reconstruction method, a fully connected network  
 358 is proposed to learn the waveform patterns from the simulation data and estimate the particle arriving time  
 359 in the experimental data. The network takes several uniformly distributed points on the leading edge of the  
 360 signal waveform as the input and outputs the length of the leading edge  $t_1$ . By subtracting  $t_1$  from the peak  
 361 time  $t_p$ , the estimated particle arriving time is  $t_a = t_p - t_1$ .

362 A preliminary cosmic ray test was conducted in Tsinghua University with two identical  $4 \times 8$  gaps  
 363 MRPCs shown in Figure 13. An amplifier with the bandwidth of 350MHz was used in this test and the  
 364 waveform digitizer was CAEN DT5742 (based on DRS4-V5 Chip). 8 uniformly distributed points from the  
 365 leading edge were obtained from the experimental data and feed into the neural network. The network was  
 366 trained and validated with 120,000 and 50,000 events respectively. Figure 14 shows the time difference of  
 367 two MRPCs and the time resolution is 27 ps. However, the amplifier used in this test was not fast enough  
 368 and the digitizers sampling rate was only  $\sim 5$ GHz. The case of MRPCs read out with a faster amplifier  
 369 (signal leading edge  $\sim 1$  ns) and a higher sampling rate ( $\sim 10$  GHz) was simulated. The result shows that  
 370 the time resolution of about 14 ps can be achieved. Recent studies on the structure of the neural network  
 371 show that using the Long-Short-Term-Memory network (LSTM) can further improve the time resolution by  
 372 about 4 ps.

373 One of the biggest challenges for the SoLID is the tremendous background rates due to the high target  
 374 luminosities which can certainly make the realistic time resolution worse than the designed performance.  
 375 Most of the background particles making into the MRPC are low-energy electrons from secondary scattering  
 376 and can be effectively removed. However, the pile-up effect will dilute the time resolution when many

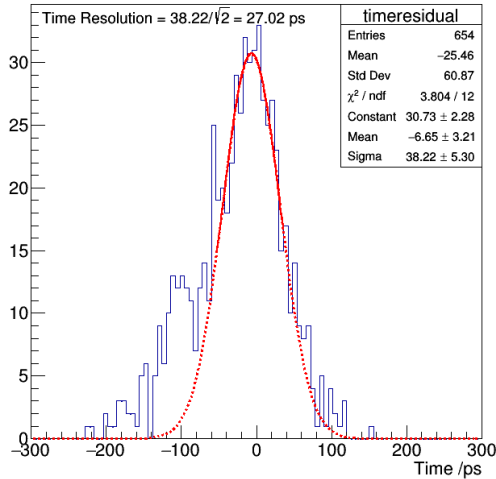


Figure 14: The time difference of two MRPCs at Tsinghua University

377 background particles come together with good particles into the same detector within the same time-window.  
 378 Several ongoing MRPC R&D projects aim for sub-picoseconds time resolution in a clean environment and  
 379 20 ps or better in high rate environments including the Tsinghua University’s study using the neural network  
 380 method. In a worse scenario, assuming the actual MRPC time resolution becomes 30 ps under the SoLID  
 381 high-rate environment, we still can use the TOF to separate  $K^\pm$  from  $\pi^\pm$  up to around 6 GeV/c above  
 382 which the event rate is already very low and the lose of kinematic phase-space is small (as shown in Fig. 24  
 383 in Section 4.1). Meanwhile, the HGC with veto signals can more effectively suppress  $\pi^\pm$  at high momenta.  
 384 Despite the challenge, we are still confident that the current R&D efforts will reach the timing resolution  
 385 requirement of this experiment before the running of SoLID.

### 386 3.6 MRPC Simulation Framework

387 To study the detector performance and design optimization, it is desired to have a digitization software.  
 388 The SoLID detector simulation is done with a GEMC Geant4 based software. A standalone post-GEMC  
 389 simulation software has been developed to optimize the MRPC design. Together with GEMC it simulates  
 390 physics processes of the MRPC as well as reconstructing time using the induced signal current. Like other  
 391 gaseous detectors, the main physics process of the MRPC is based on ionization. When a charged particle  
 392 passes through a gas volume, it ionizes gas atoms which can result in electron-ion pair production. A primary  
 393 electron with enough energy can further ionize other atoms. In a very high electric field, it can create an  
 394 electron avalanche and induce a signal on the electrodes.

395 Figure 15 shows an overview of the simulation procedure. The output of the GEMC simulation provides  
 396 information on the physics hits. The detector response is characterized by transport parameters such as  
 397 Townsend (avalanche) coefficient  $\alpha$ , attachment coefficient  $\eta$  and electron drift velocity  $v$ . The parameters  
 398 are obtained using the MAGBOLTZ program for an operating voltage of 6.6 kV which gives  $E = 108$  kV/cm.  
 399 For the SoLID MRPC simulation we used the following parameters:  $\alpha = 129/\text{mm}$ ,  $\eta = 5.435/\text{mm}$ , and  $v =$   
 400  $0.201$  mm/ns.

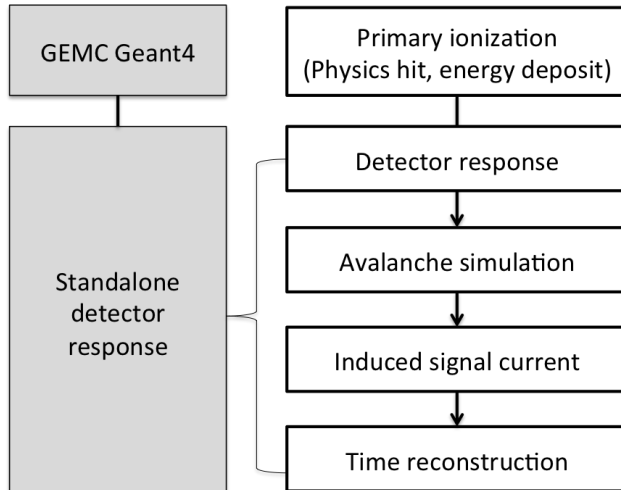


Figure 15: Schematic of the MRPC simulation

401 The electron multiplication (avalanche) process is simulated using a 1-Dimensional avalanche gas model  
 402 developed by W. Riegler, C. Lippmann, and R. Veenhof [46]. The model allows an efficient avalanche  
 403 simulation. In the simulation, an electron starts an avalanche that will grow until they reach to the end  
 404 of the gas gap. Considering an electron at a position  $x$  in an gap, one can calculate the probability for an  
 405 avalanche started with a single electron to contain  $n$  electrons at  $x+dx$  as:

$$P(n, x) = \begin{cases} k \frac{\bar{n}(x)-1}{\bar{n}(x)-k} & (n=0) \\ \bar{n}(x) \left( \frac{1-k}{\bar{n}(x)-k} \right)^2 \left( \frac{\bar{n}(x)-1}{\bar{n}(x)-k} \right)^{n-1} & (n>0) \end{cases}$$

406 where the average number of electrons is  $\bar{n}(x) = e^{(\alpha-\eta)x}$ , and  $k = \eta/\alpha$ . For each gas layer, the gap is  
 407 divided into 200 steps, and for each step  $dx$ , the number of electrons with a probability for ionization and  
 408 attachment is calculated. The same process is repeated over all electrons within a given gap until they reach  
 409 to the end of the gap. In addition, we employ an effective model based on the central limit theorem once  
 410 the number of electrons is sufficiently large ( $n > 200$ ) in order to reduce computing time. In such a case, the  
 411 number of electrons at  $x + dx$  can be obtained by sampling a random number from a Gaussian with a mean  
 412 of  $\mu = n\bar{n}(dx)$  and  $\sigma = \sqrt{n}\sigma(dx)$ . Note that this 1-D model does not take into account that the growth of the  
 413 avalanche is affected by space charge. The space charge effect stops exponential avalanche growth. In this  
 414 simulation, we take the space charge effect into account by applying a simple cut-off to the avalanche size.  
 415 Once the number of electrons exceeds  $1.5 \cdot 10^7$ , the avalanche size will be saturated as shown in Fig. 16. As  
 416 it can be seen from panel b we obtain a very reasonable agreement between the simulation and the effective  
 417 model.

418 The induced current signal is then calculated using Ramo's theorem [47]:

$$i(t) = E_w \cdot v \cdot e_0 \cdot N(t) \quad (20)$$

419 where  $E_w$  is the weighting electric field,  $v$  is the electron drift velocity,  $e_0$  is the electron charge, and  $N(t)$  is  
 420 the number of electrons at time  $t$ . The weighting field is calculated using the number of gas gaps, the width

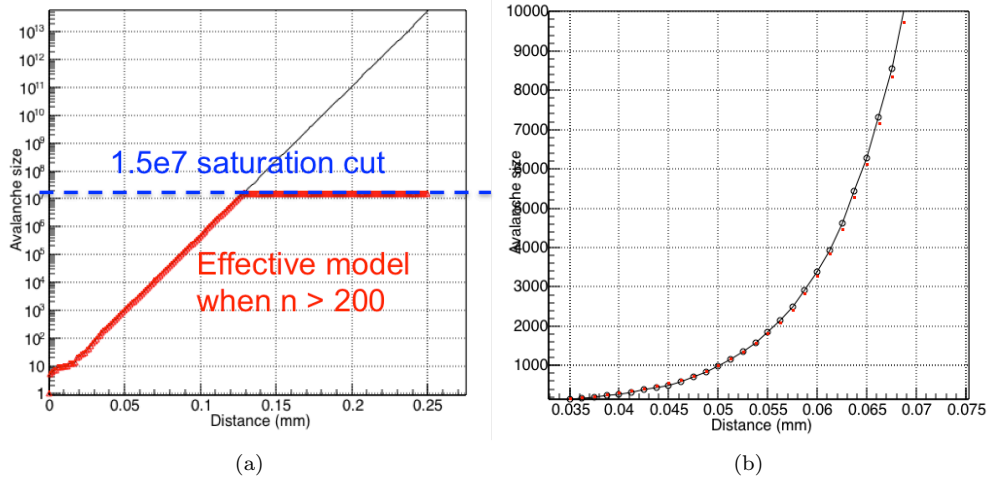


Figure 16: Simulated avalanche size from an electron as a function of the distance from the entrance of the gap for (a) the full gap width and (b) a zoomed-in for a region close to the entrance of the gap. Black circles show the simulated avalanche size, and the red circles show the avalanche size from the effective model when  $n > 200$ . The blue dashed line shows a saturation cut-off.

421 of gaps and other material plates, and permittivity of the resistive plates. Lastly, the timing information is  
 422 obtained using a leading edge discriminator.

423 In addition to the gas transport parameters, the simulation is further tuned to match with the cosmic  
 424 test result. A Gaussian noise in the signal processing is introduced with  $\sigma_{noise}$ , and an additional smearing  
 425 factor for the timing of  $\sigma_{smear}$  are applied to match the simulation output with the data. Both the time and  
 426 integrated charge are recorded for each particle that enters the MRPC volume. The time-walk correction is  
 427 then performed to get the timing resolution. The time-walk correction function used can be defined as:

$$f(Q) = c_0 + \frac{c_1}{\sqrt{Q}}. \quad (21)$$

428 Figure 17 (c) shows a time distribution after the time-walk correction from a single muon simulation. The  
 429 resolution of about 49 ps is obtained in the simulation which is similar to the one from the cosmic test with  
 the prototype design.

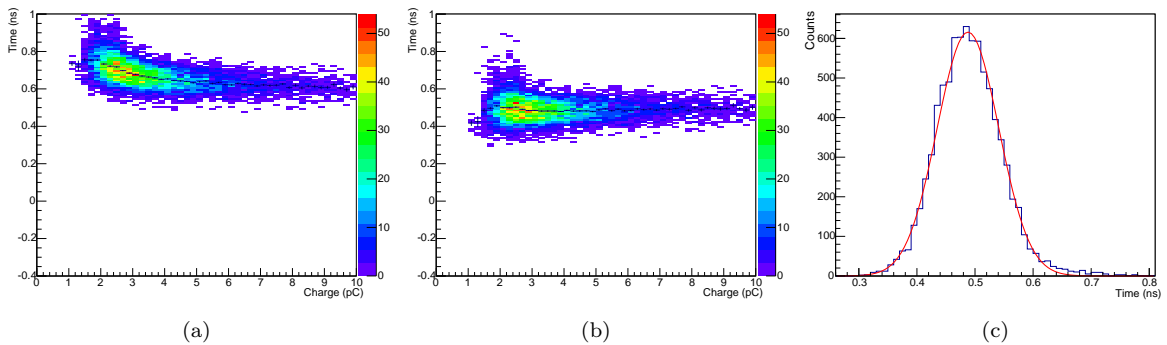


Figure 17: Time-charge correlation: (a) before time-walk correction and (b) after the correction. (c) Timing distribution after time-walk correction. The obtained time resolution from a Gaussian fit is  $\approx 49$  ps.

### 3.7 Kaon Identification with TOF and HGC

Using the simulation software, preliminary studies have been performed for  $\pi^\pm$  and  $K^\pm$ . In this study, single  $K^-$  and  $\pi^-$  were generated for various momentum settings. The smearing factor is adjusted in the simulation in order to set the time resolution to  $\sim 20$  ps. The average  $\pi^-/K^-$  ratio estimated using the SIDIS MC (see Section 4.2 for details) is around 10. The ratio is larger at low momenta, but the pion rate drops more quickly as the momentum increases. The ratio reduces to around 3 at the momenta of 4-6 GeV/c. The HGC can further reduce the pion rates by vetoing pion signals at momenta above its threshold as discussed in Section 3.2. In the simulation study, the pion yield is scaled according to the reduced  $\pi^-/K^-$  ratio. From the kaon  $\Delta t$  ( $= t_{MRPC} - t_{expected}^{kaon}$ ) distribution the peak and sigma values are extracted, and a  $\pm 3\sigma$  TOF cut is applied to estimate the pion contamination.

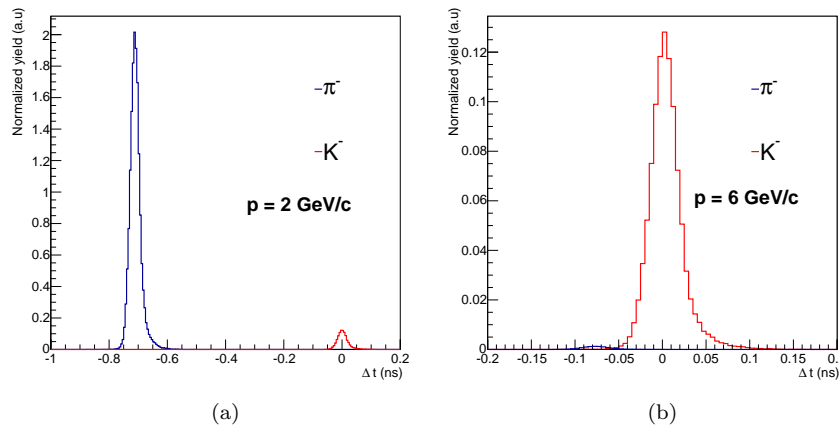


Figure 18: Time difference distributions between the MRPC time and the expected Kaon signal time for the momentum of 2 GeV/c (left) and 6 GeV/c (right). The time resolution of 20 ps is assumed. The pion yields are scaled using the expected  $\pi^-/K^-$  ratio and pion rejection factor from the HGC. The total scale factors of 16 and 0.01 are used for 2 GeV/c and 6 GeV/c, respectively.

Figure 18 shows simulated  $\Delta t$  distributions for momenta of 2 and 6 GeV/c. For 2 GeV/c where the momentum is below the pion Čerenkov threshold ( $\sim 2.2$  GeV), we scaled the pion yield by the  $\pi^-/K^-$  ratio of 16 that is estimated by the SIDIS MC. At this momentum, the MRPC can separate  $K^\pm$  from  $\pi^\pm$  very well as shown in Fig. 18 (a). The MRPC even with an 80 ps time resolution can provide enough separation power at this momentum. At higher momenta, it is important to suppress the pion background due to relatively limited separation power of the TOF. Assuming the HGC reduces  $\pi^- : K^-$  to 1:100 at the momentum of 6 GeV/c and the time resolution of 20 ps, the pion contamination is estimated as  $\sim 0.1\%$  from Fig. 18 (b). For the time resolution around 30 ps, the pion contamination would still be less than 1% for high momentum region (4-6 GeV/c) without taking into account other background effects.

As discussed in section 3.5 there have already been several MRPC detector designs that have demonstrated a timing resolution below 20ps. Together with the detailed studies performed at Tsinghua University we plan to use the simulation framework described above to cross-check results and guide future detector design. A detailed simulation is currently underway and will produce results in the near future for the updated MRPC. The final detector design will take into consideration realistic high-rate background effects.



## 4 Projected Results

The kinematic coverages and projected results were produced based on exactly the same detector setup of the transversely polarized  $^3\text{He}$  target experiment (E12-10-006 [19]) and the transversely polarized proton target experiment (E12-11-108 [20]). We also applied the same target luminosities and the approved beam-time. As discussed in Section 3, a time resolution of 20 ps should allow us to separate  $K^\pm$  from  $\pi^\pm$  up to a maximum momentum of 7 GeV/c. To be shown later, the maximum momentum of  $K^\pm$  in the SIDIS reaction at 11 GeV is about 7.5 GeV/c without the  $0.3 < z < 0.7$  cut (and becomes 6.5 GeV/c with the  $z$  cut). It means that the requirement on the timing resolution should be sufficient.

The Monte-Carlo generator used in this study is the updated version of our standard SIDIS generator which has been widely used in the original three SoLID-SIDIS proposals, the SoLID pCDR [32], and our Transversity projection paper [48]. We have updated the unpolarized SIDIS cross section model [49] using the CJ15 PDF sets [50] and DSS LO Fragmentation Functions [51]. While the older model in this generator was fine-tuned using the 6 GeV Hall A pion transversity data, this new model gives better agreement with the HERMES results and provides a better estimation of the  $K^\pm$  production. Note that the following kinematic cuts were applied when generating the simulated events to only select DIS events:  $Q^2 > 1 \text{ GeV}^2$ ,  $W > 2.3 \text{ GeV}$ , and  $W' > 1.6 \text{ GeV}$ .

### 4.1 Kinematic Coverage

Following our conventional way of performing the SIDIS simulation, we produced the SIDIS events uniformly in a kinematic phase-space which is slightly wider than the actual designed range, then calculated the weight of each event based on its unpolarized cross section normalized by target luminosities and approved beam-time. The event-by-event weight was further folded in the acceptance probabilities of the electrons and  $K^\pm$  in this event. The most updated detector acceptance profiles using the CLEO-II solenoid magnet were created from our GEMC simulation. Fig. 19, Fig. 20 and Fig. 21 show the acceptance of electrons and  $K^\pm$  in both the  $\text{NH}_3$  and  $^3\text{He}$  configurations, respectively. Note that for the  $\text{NH}_3$  setup, there are certain regions where the rates are very high due to the "sheet of flames" issue caused by the interference between the strong DNP target magnet field and the solenoid magnet field. The detectors in these regions are disabled and that causes the gaps in the azimuthal angular coverage.

The kinematic coverage of the Kaon-SIDIS production are shown in Fig. 22 and Fig. 23. As discussed in the previous section, the maximum momentum range of  $K^\pm$  can be affected by the time resolution of the MRPC. Fig. 24 shows that when  $P_K > 6 \text{ GeV}/c$  the correlations between kaon momenta and important physics quantities,  $Q^2$ ,  $z$ ,  $p_T$  and  $x_B$ , are less important, so the effect will be minimum if a worse time resolution (30 ps) forces us to cut out these physics regions.

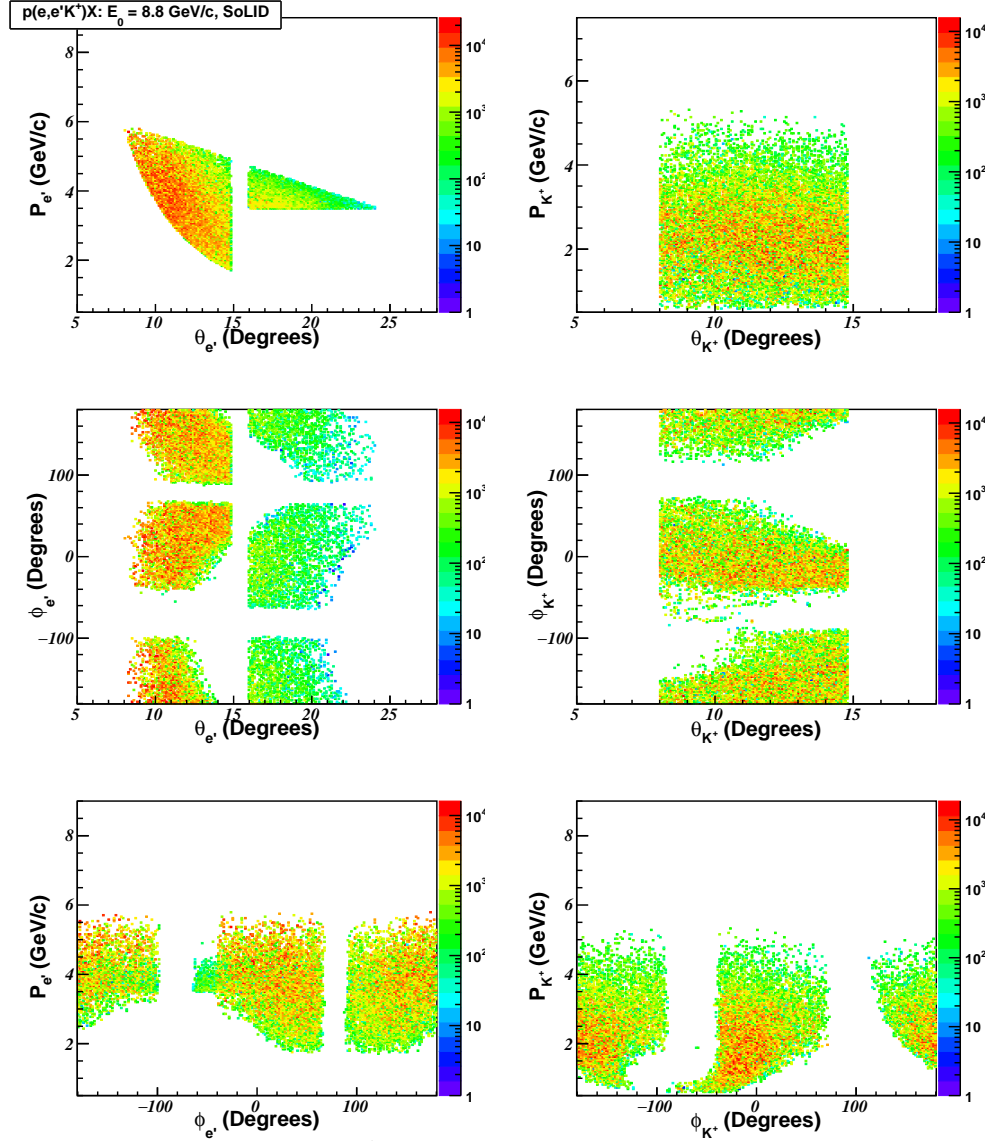


Figure 19: The acceptances of electrons and  $K^+$  from the SIDIS reaction at 8.8 GeV using the NH<sub>3</sub> target and the SoLID (simulated by GEMC). The gaps in  $\phi_{e'}$  and  $\phi_{K^\pm}$  are the cut-off regions where the 5T transverse NH<sub>3</sub> target magnet field and the 1.4T longitudinal solenoid magnet field create high background in narrow bands of azimuthal angles.

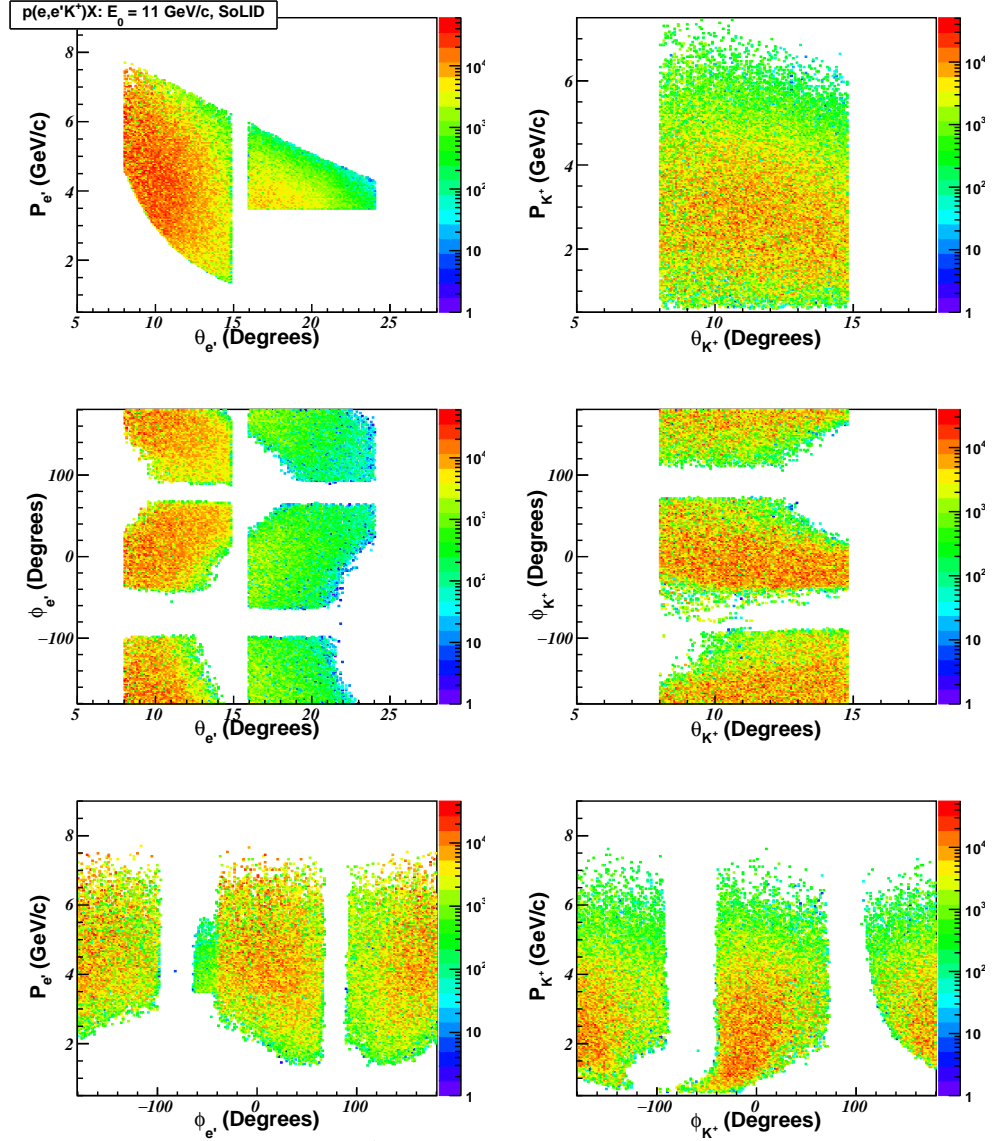


Figure 20: The acceptances of electrons and  $K^+$  from the SIDIS reaction at 11 GeV using the  $\text{NH}_3$  target and the SoLID (simulated by GEMC). The gaps in  $\phi_{e'}$  and  $\phi_{K^\pm}$  are the cut-off regions where the 5T transverse  $\text{NH}_3$  target magnet field and the 1.4T longitudinal solenoid magnet field create high background in narrow bands of azimuthal angles.

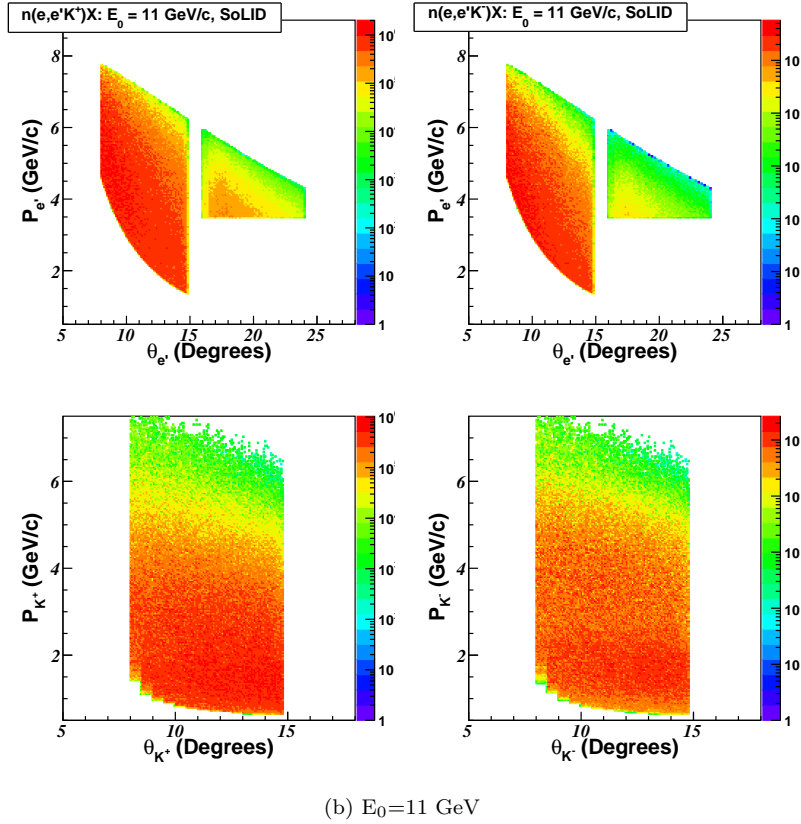
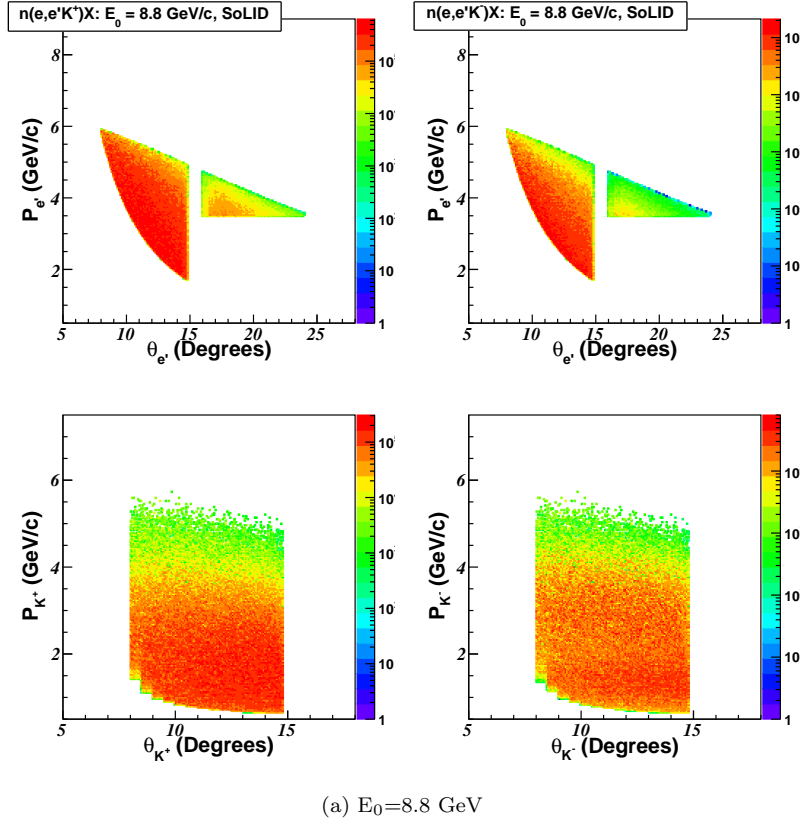
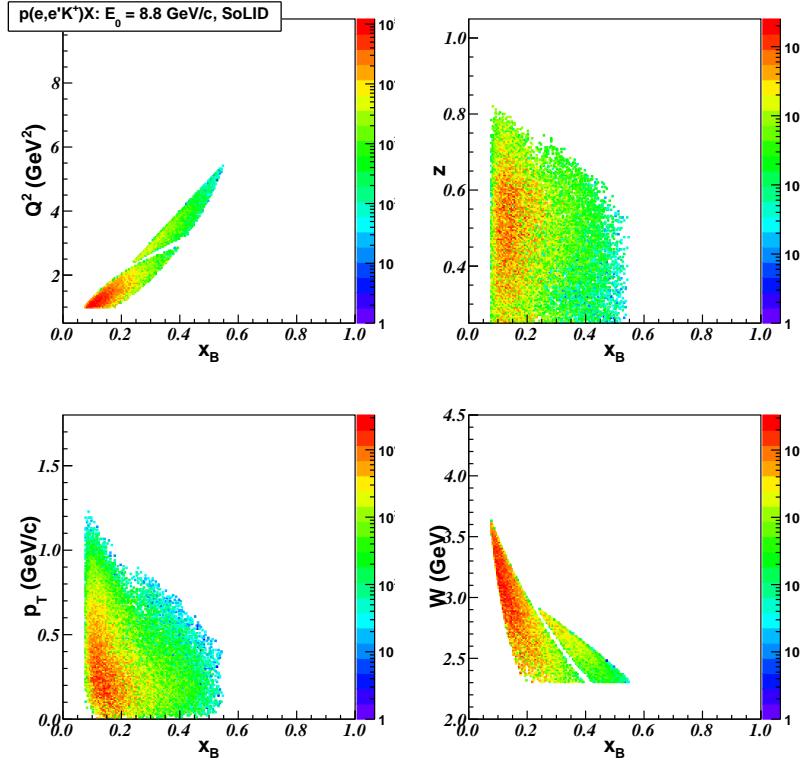
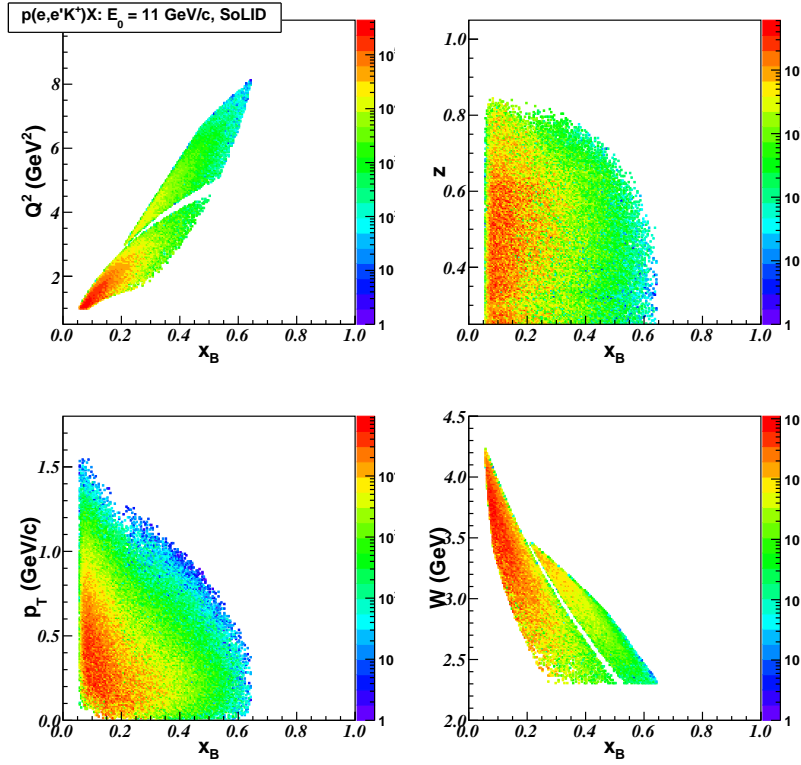


Figure 21: The acceptances of electrons and  $K^+$  from the SIDIS reaction: at 8.8 GeV (top) and 11 GeV (bottom) using the  $^3\text{He}$  target and the SoLID (simulated by GEMC).

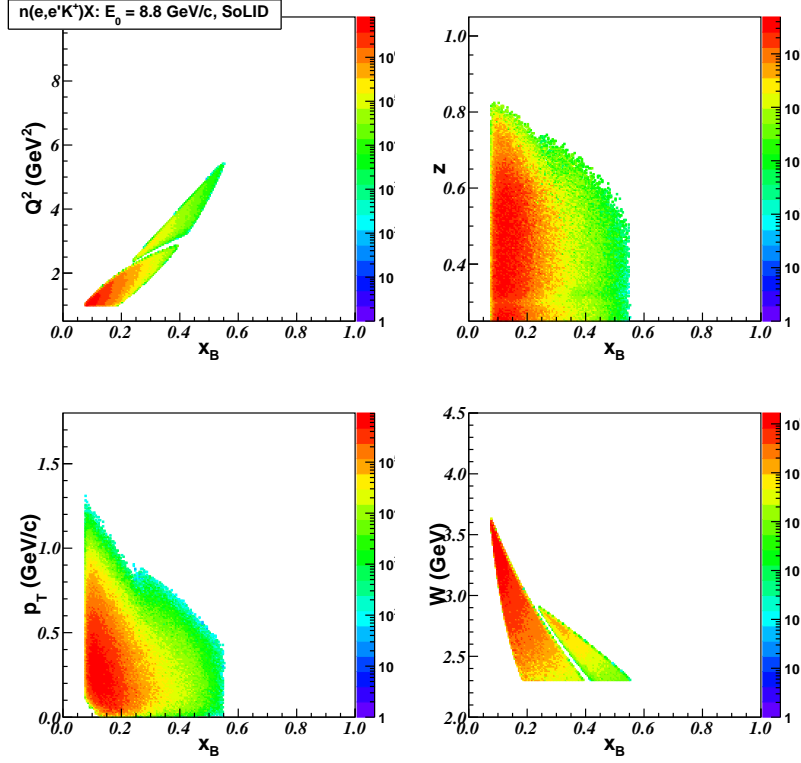


(a)  $E_0=8.8$  GeV

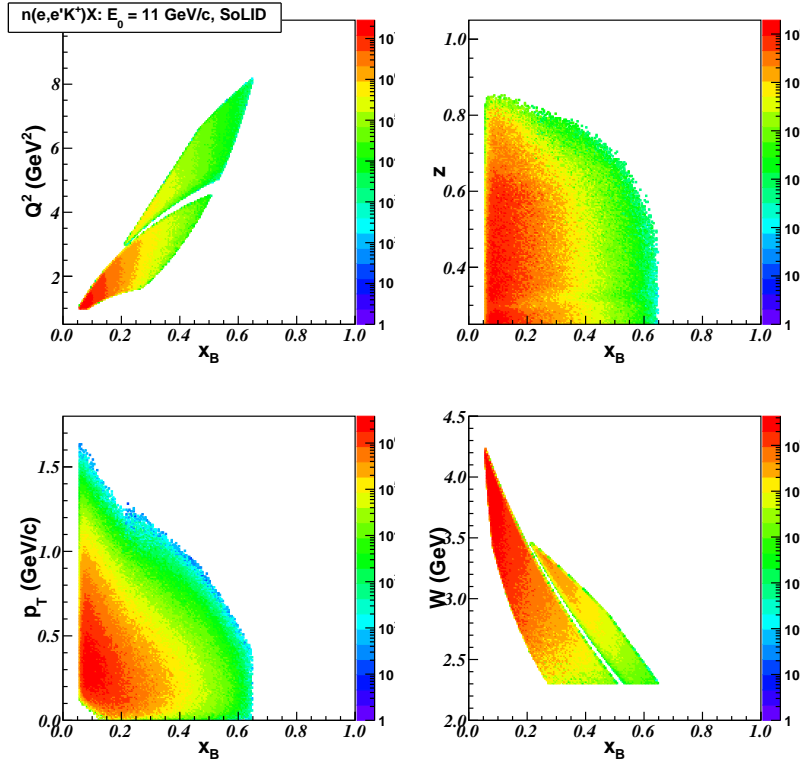


(b)  $E_0=11$  GeV

Figure 22: The kinematic coverage of the Kaon-SIDIS production with the NH<sub>3</sub> target and the 8.8 GeV (top) and 11 GeV (bottom) electron beam.



(a)  $E_0=8.8 \text{ GeV}$



(b)  $E_0=11 \text{ GeV}$

Figure 23: The kinematic coverage of the Kaon-SIDIS production with the  $^3\text{He}$  target and the 8.8 GeV (top) and 11 GeV (bottom) electron beam. Unlike the  $\text{NH}_3$  setup, the  $^3\text{He}$  setup provides a full coverage of the azimuthal angles for both  $\phi_{e'}$  and  $\phi_{K^\pm}$ .

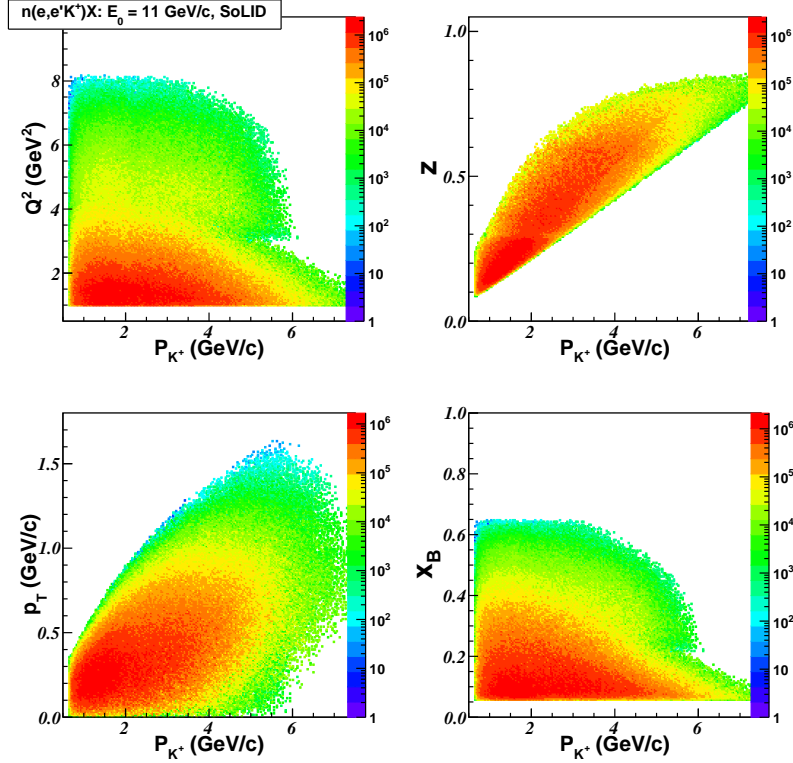


Figure 24: The correlations of  $K^\pm$  momenta vs important physics quantities using the  $^3\text{He}$  target at 11 GeV.

487 **4.2 Rate Estimations**

SoLID-SIDIS Coincident Rates (Hz)				
Polarized Target	$^3\text{He}$ ("n")		$\text{NH}_3$ ("p")	
Beam Energy	8.8 GeV	11 GeV	8.8 GeV	11 GeV
e-(FAEC+LAEC)+ $K^+$ (FAEC)	359.3	575.6	4.9	10.4
e-(LAEC+LAEC)+ $K^-$ (FAEC)	83.2	144.1	0.93	2.7
e-(FAEC+LAEC)+ $\pi^+$ (FAEC)	1555.0	2185.9	20.3	37.4
e-(LAEC+LAEC)+ $\pi^-$ (FAEC)	1012.5	1449.6	10.2	20.7

Table 1: Estimated Rates of the Kaon-SIDIS production with  $^3\text{He}$  (neutron) and  $\text{NH}_3$  (proton) targets at 8.8 GeV and 11 GeV beam energies. The pion rates are also given here as comparison.

488 The rate estimation was performed using the SIDIS MC events weighted by the unpolarized kaon cross sec-  
 489 tions, target luminosities, and the SoLID-SIDIS acceptance profiles. We used the designed target luminosity  
 490 of  $1 \cdot 10^{35} \text{ cm}^{-1} \text{ s}^{-1}$  per target for  $\text{NH}_3$  and  $1 \cdot 10^{36} \text{ cm}^{-1} \text{ s}^{-1}$  per target for  $^3\text{He}$ , respectively. A cut,  
 491  $0.3 < z < 0.7$ , was applied in addition to the kinematic cuts mentioned above. As a comparison and a  
 492 cross check, the pion rates are also listed here which were calculated with the same generator and the same  
 493 procedure. The pion rates are consistent with our previous estimations in the SoLID pCDR [32] where we  
 494 used an older cross section model.

### 4.3 Projected Asymmetries

We combined the 8.8 GeV and 11 GeV simulation data together and used the corresponding approved beam-time of the pion measurements with both polarized targets. We then binned the data in terms of 4D ( $Q^2$ ,  $z$ ,  $P_{hT}$ ,  $x_B$ ) and calculated the statistical uncertainties of the  $K^\pm$  measurements. The procedure of binning the data and calculating numbers of events in each bin is identical to the one used in obtaining the most updated projection results of the pion measurements. The main differences are the models that calculate kaon unpolarized cross sections. We also used the more up-to-date detector acceptance profiles. On the other hand, since the  $K^\pm$  rates are much lower than the pion's, we had to enlarge the bin sizes of  $Q^2$ ,  $z$  and  $p_T$ , which are now defined by the following:

$$Q^2 \text{ bins}[3] = (1.0 - 2.0), (2.0 - 4.0), (4.0 - 10.0), \text{ in GeV}^2, \quad (22)$$

$$z \text{ bins}[4] = (0.3 - 0.4), (0.4 - 0.5), (0.5 - 0.6), (0.6 - 0.7), \quad (23)$$

$$P_{hT} \text{ bins}[5] = (0.0 - 0.2), (0.2 - 0.4), (0.4 - 0.6), (0.6 - 1.0), (1.0 - 1.6), \text{ in GeV}/c. \quad (24)$$

The way to determine the  $x_B$ -bins is the same as the one in the pion measurements where we require the maximum statistical error in each bin to be  $\leq 5\%$ . The experimental observable of this measurement is the single spin asymmetry (SSA) with an unpolarized electron beam and transversely polarized target, which is defined as:

$$A_{UT}(Q^2, z, p_T, x_B, \phi, \phi_S) = \frac{1}{f_d P_t} \cdot \frac{N^\uparrow - N^\downarrow}{N^\uparrow + N^\downarrow}, \quad (25)$$

where  $N^{\uparrow(\downarrow)}$  corresponds to the number of events with the target spin orientation in two opposite directions, (e.g., up (down)).  $f_d$  is the dilution factor calculated bin-by-bin using our model as being used in our previous pion SIDIS proposals, and  $P_t$  is the polarization of the target. For protons in  $\text{NH}_3$ ,  $f_d$  is roughly 0.13 and  $P_t$  is set to be 70%. For neutrons in  $^3\text{He}$ ,  $f_d$  is between 0.15 to 0.3 and  $P_t$  is 65%  $\cdot$  86.5%. Note that during the projection study we set  $A_{UT}$  to be constantly zero for all bins since their amplitudes are small and not well determined theoretically and experimentally. We are interested in the relative statistical uncertainty of each bin which is defined as:  $\delta A_{UT} = 1/\sqrt{(N^\uparrow + N^\downarrow)/2}$ . Let's define  $N = (N^\uparrow + N^\downarrow)/2$  as the number of events with unpolarized (or spin-average) target orientation, then in our simulation, we can calculate its value for each ( $Q^2$ ,  $z$ ,  $p_T$ ,  $x_B$ ) bin:

$$N = \left( \sum_{i \in \text{bin}} \sigma_i^{avg} \cdot Acc_i^{(e'+K^\pm)} \right) \cdot PSF/N_{gen} \cdot T_{8.8\text{GeV}(11\text{GeV})} \cdot Lumi \cdot \epsilon_{det,eff}, \quad (26)$$

where  $\sigma_i$  is the unpolarized SIDIS cross section per target,  $Acc_i^{(e'+K^\pm)}$  is the product of the electron acceptance and  $K^\pm$  acceptance in SoLID. They vary event-by-event.  $PSF$  and  $N_{gen}$  are the total phase-space and the number of total generated MC events defined in the GetSIDIS generator.  $T_{8.8\text{GeV}(11\text{GeV})}$  is number of the approved beam-time (in seconds) on  $\text{NH}_3$  or  $^3\text{He}$  targets at 8.8 GeV or 11 GeV electron beam energy.  $T_{8.8\text{GeV}} = 29$  days and  $T_{11\text{GeV}} = 56.5$  days for  $\text{NH}_3$ , and  $T_{8.8\text{GeV}} = 21$  days at and  $T_{11\text{GeV}} = 48$  days for  $^3\text{He}$ .  $Lumi$  is the luminosity of the targets and their numbers can be found in Section 4.2.  $\epsilon_{det,eff}$  is the total detector efficiency of detecting electrons and kaons which are set to be 85%, respectively.

With the real experimental data, we can further decompose the SSA into different modules with different



525 azimuthal angular dependences which correspond to different TMD contributions as discussion in Section I:

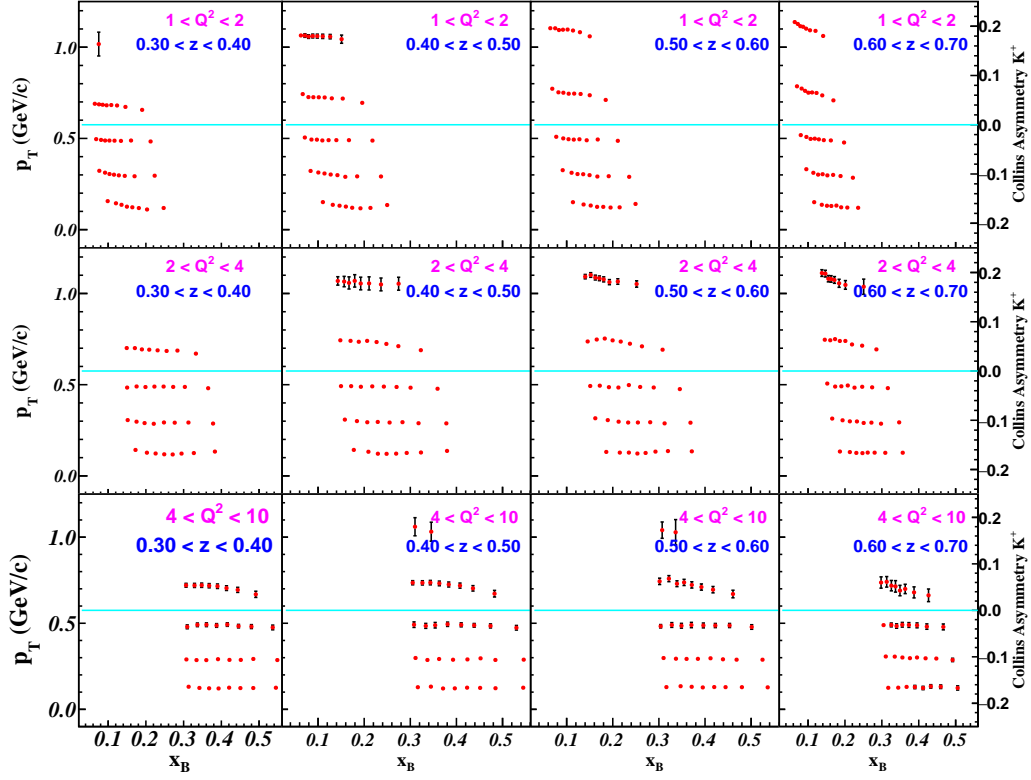
$$A_{UT} = A_{UT}^{Collins} \sin(\phi + \phi_S) + A_{UT}^{Sivers} \sin(\phi - \phi_S) + A_{UT}^{Pretzelocity} \sin(3\phi - \phi_S) + \dots, \quad (27)$$

526 In this projection, we also estimated the effect of the incomplete azimuthal angular coverage to the  
 527 total uncertainties when extracting Collins, Sivers, and Pretzelocity asymmetries. The full  $4\pi$  coverage  
 528 of the SoLID detector results in this effect to be mostly at few percentage levels for the  $^3\text{He}$  setup while  
 529 it can be slightly larger for the  $\text{NH}_3$  setup due to the azimuthal gaps. The effect only becomes large at  
 530 certain kinematic regions where the azimuthal angles are partially covered. The impact of this effect was  
 531 added as a correction factor for each bin on top of the bin-by-bin statistical uncertainty when presenting  
 532 uncertainties of individual asymmetries. The projected results are given in Fig. 25 for extracting the Collins  
 533  $K^\pm$  asymmetries for the  $^3\text{He}$  target. The results for the Sivers asymmetries are similar as shown in Fig. 26.  
 534 We totally obtained near 430 bins in 4D with uncertainties mostly less than 1% thanks to the higher target  
 535 luminosity. Some high  $p_T$  points have significantly large error bars due to the large correction factors (up  
 536 to 3) for limited azimuthal angular coverage. The uncertainties for the  $\text{NH}_3$  setup, especially for  $K^-$ , are  
 537 much larger under the 4D binning due to the low production rates. We integrated over the  $Q^2$  range and  
 538 only performed the 3D ( $z, p_T, x_B$ ) binning, as shown in Fig. 27 and Fig. 28. We obtained roughly 120 bins  
 539 in 3D with most uncertainties less than 5%. The projected coverage and uncertainties are greatly improved  
 540 compared with the HERMES and COMPASS data. They are also significantly better than the CLAS12  
 541 proposal (C12-11-111 [22]) which only binned in 2D ( $p_T, x_B$ ). During the real data analysis, the binning  
 542 methods on both targets can be systematically optimized based on the actual rates and acceptance.

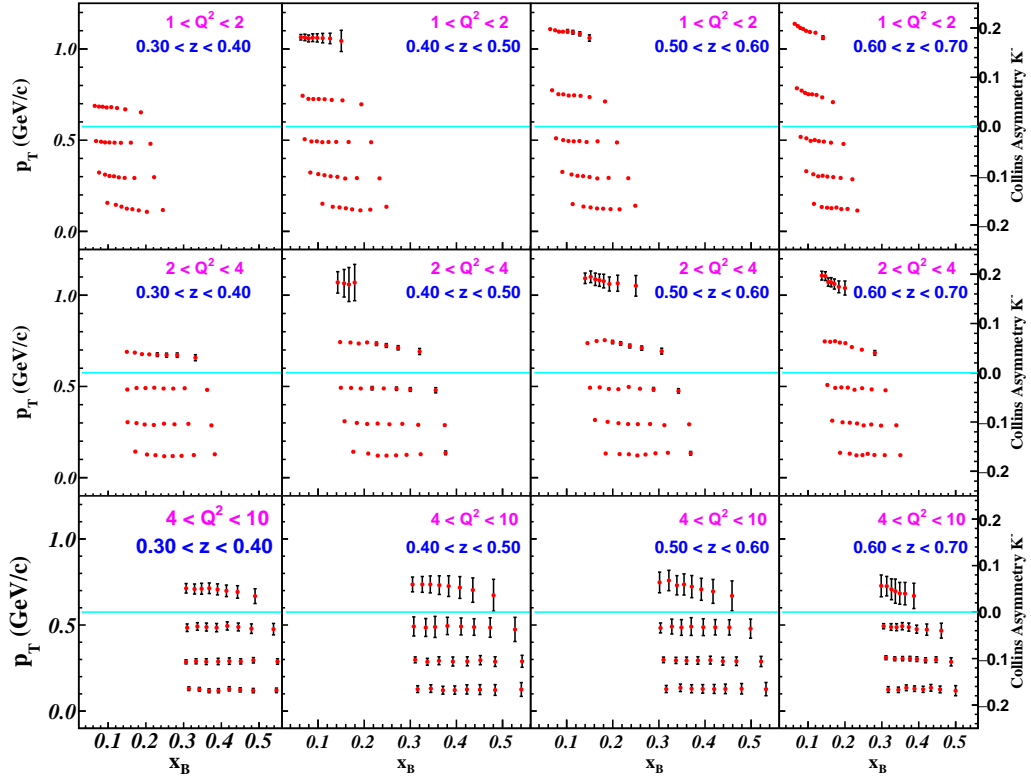
543 The projection of the Pretzelocity asymmetry is not shown here. The model prediction of the pion  
 544 Pretzelocity asymmetry is only at the level of sub-percentage, and hence we had to bin the data only in  
 545 the  $x_B$  dimension to obtain the statistical uncertainties at such level. Because the prediction of the kaon  
 546 Pretzelocity asymmetry is yet available, any projection won't be useful, especially due to the very low  $K^\pm$   
 547 production rates. However, during the real data analysis, we will still extract this asymmetry together with  
 548 other asymmetries and study its actual amplitude.

549 We would like to stress that the total SSA in Eq. 25 (or Eq. 27) are our major experiment observables  
 550 and for now we don't attempt to make any direct connections to individual TMDs. As discussed in Section  
 551 1.4, a theoretical model suggests that only 20% of our SoLID kaon data are under the current fragmentation  
 552 region. We require a cleaner theoretical definition of the kaon fragmentation region when the future data  
 553 become available for the TMD extraction.

554 In the approved SoLID-SIDIS proposal [19, 20, 33], the measurement of double spin asymmetries (DSA)  
 555 in the  $\pi^\pm$  production was also proposed with an additional requirements on the longitudinally polarized  
 556 electron beam and the both longitudinally and transversely polarized targets. The  $\pi^\pm$  DSA asymmetries are  
 557 related to other TMD functions such as the Helicity TMD ( $g_{1L}$ ) and two Worm-Gear TMDs ( $g_{1T}$  and  $h_{1L}^\perp$ )  
 558 which provide unique sensitivity to the orbital angular momentum (OAM) of valence-quarks. Although in  
 559 this proposal our main physics goal is to extract the  $K^\pm$  Collins, Sivers and Pretzelocity asymmetries using  
 560 transversely polarized targets, we leave the opportunity open to also measure the DSA in  $K^\pm$  production  
 561 with both transversely and longitudinally polarized targets to study the OAM of sea-quarks. The work  
 562 can be a standalone run-group proposal in the near future or can be carried out simultaneously with this  
 563 proposed measurement.

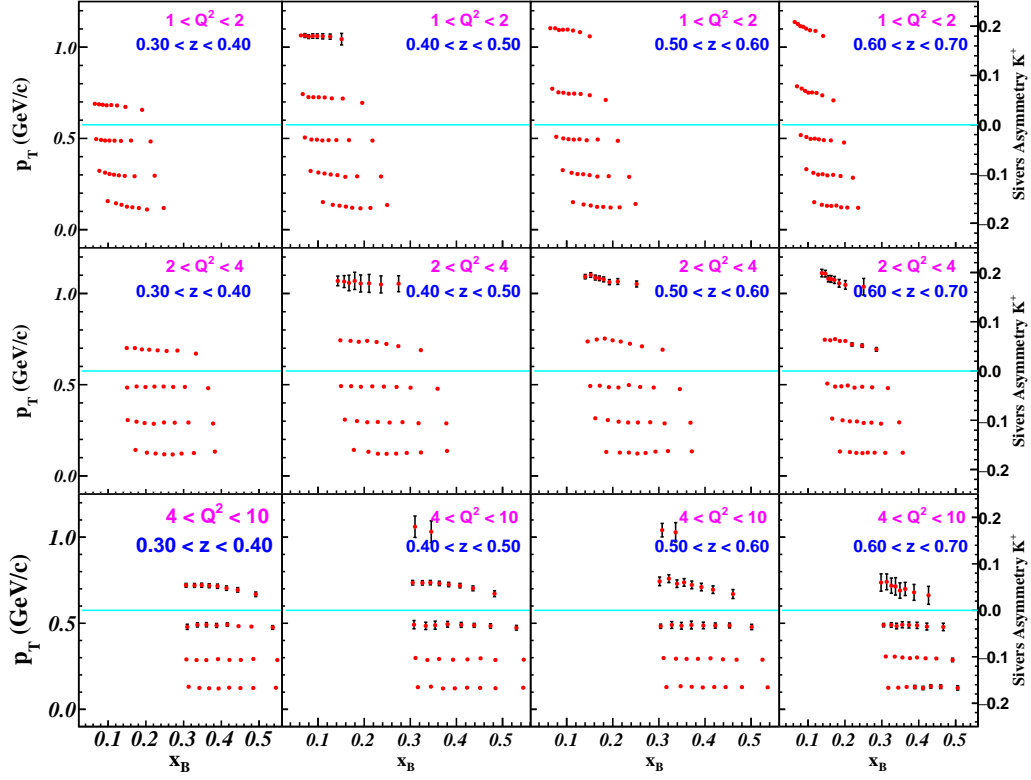


(a)  $\bar{n}(e, e'K^+)X$

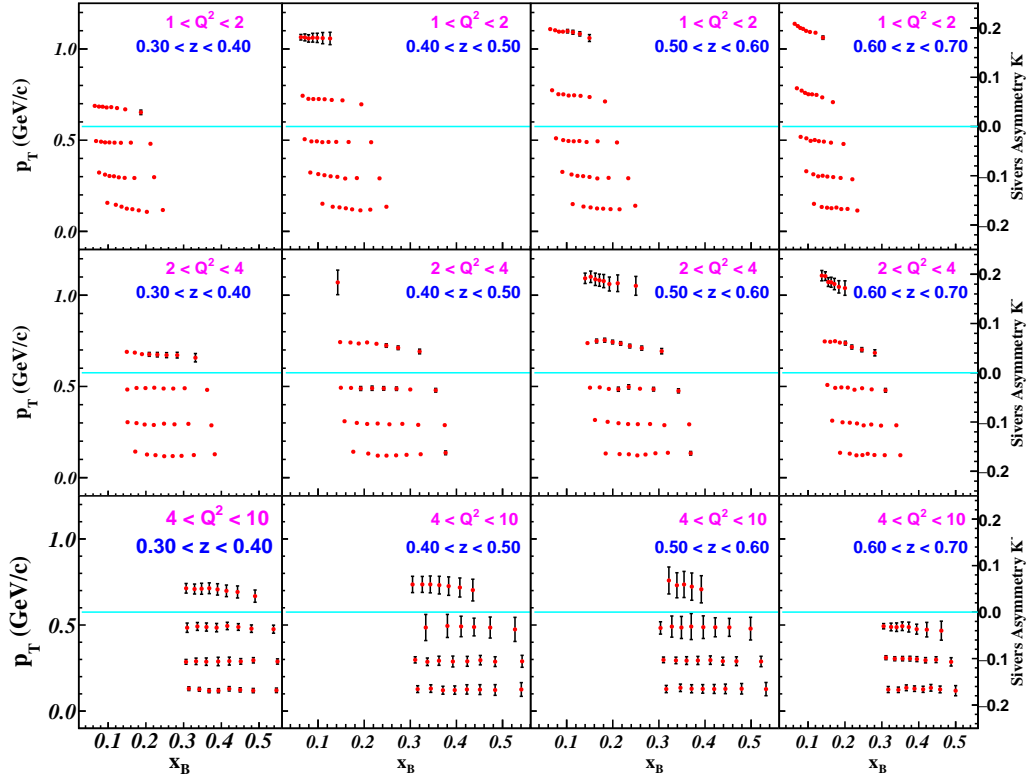


(b)  $\bar{n}(e, e'K^-)X$

Figure 25: The 4D ( $Q^2, z, p_T, x_B$ ) binning projection and statistical uncertainties of the  $K^\pm$  Collins asymmetry ( $A_{UT}^{\sin(\phi+\phi_S)}$ ) for the transversely polarized  $^3\text{He}$  (neutron) target after combining the 11 GeV and 8.8 GeV simulation data. The sizes of the uncertainties are indicated by the Y axis on the right.

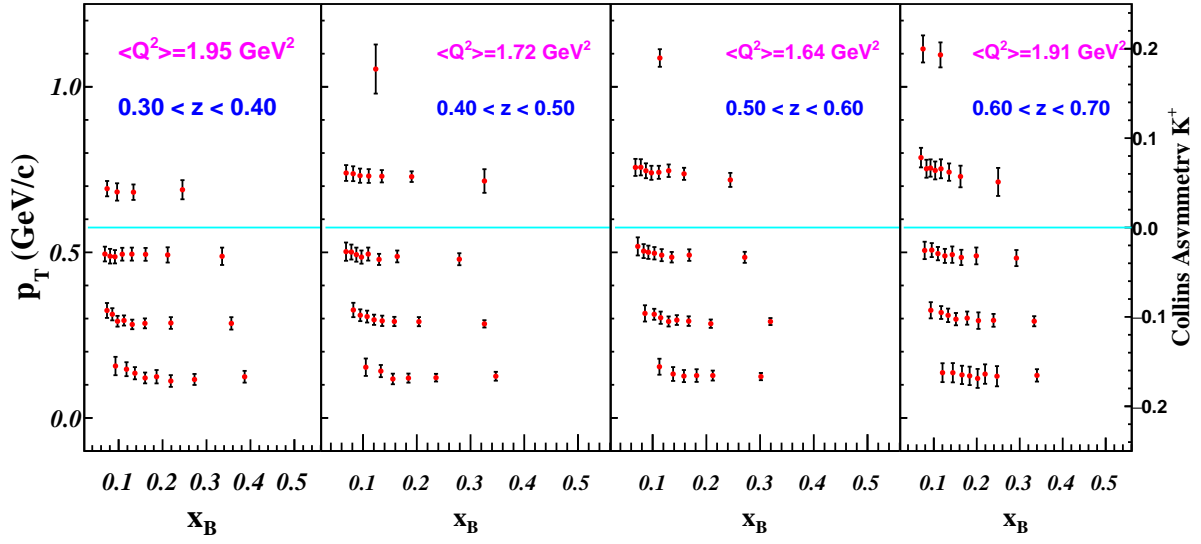


(a)  $\bar{n}(e, e' K^+)X$

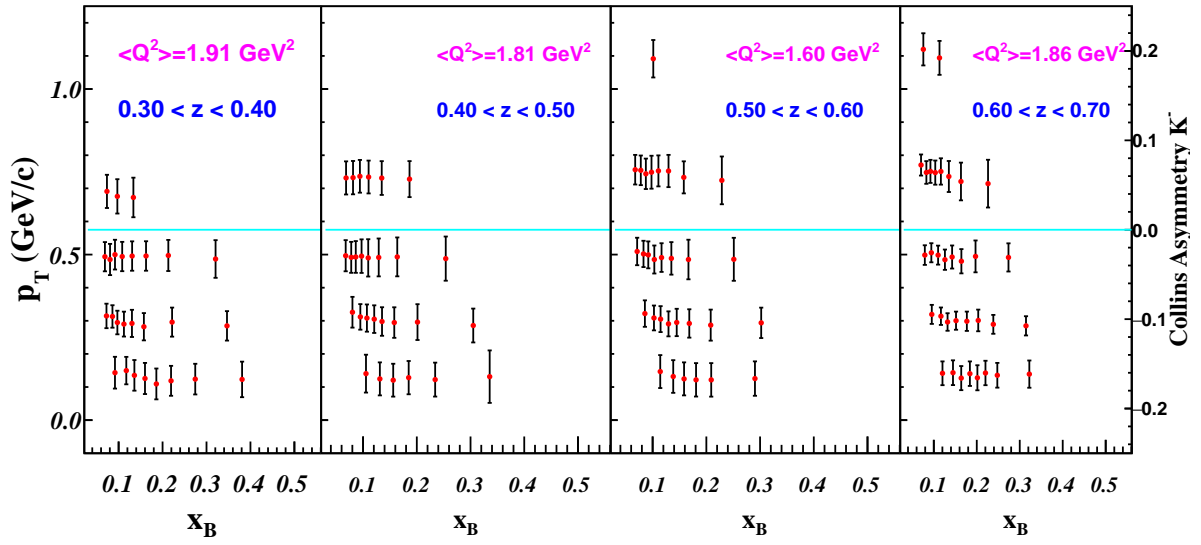


(b)  $\bar{n}(e, e' K^-)X$

Figure 26: The 4D ( $Q^2$ ,  $z$ ,  $p_T$ ,  $x_B$ ) binning projection and statistical uncertainties of the  $K^\pm$  Siverts asymmetry ( $A_{UT}^{\sin(\phi-\phi_S)}$ ) for the transversely polarized  $^3\text{He}$  (neutron) target after combining the 11 GeV and 8.8 GeV simulation data. The sizes of the uncertainties are indicated by the Y axis on the right.

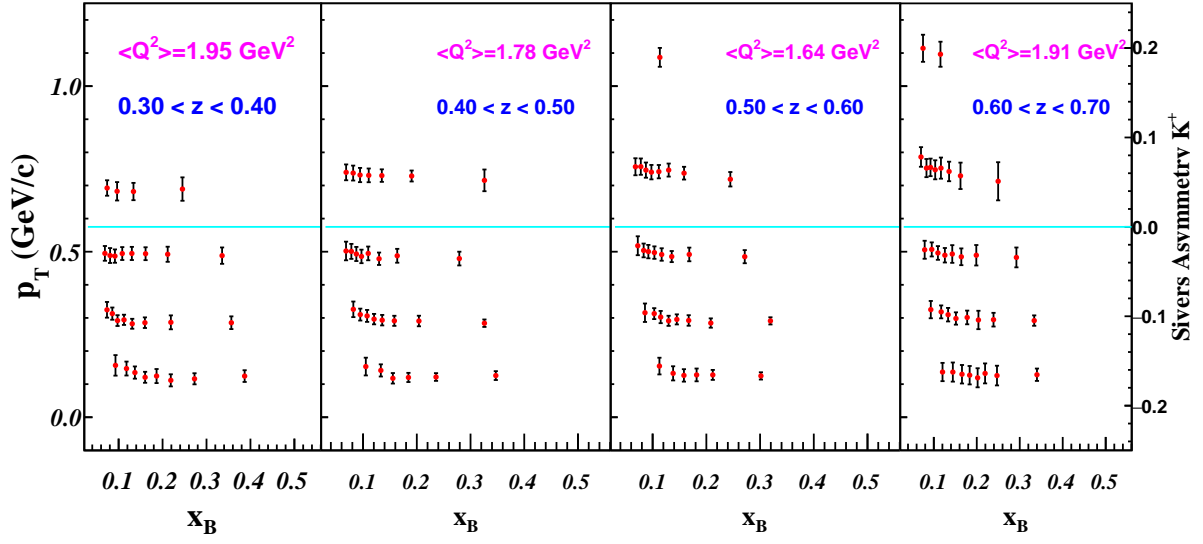


(a)  $\bar{p}(e, e'K^+)X$

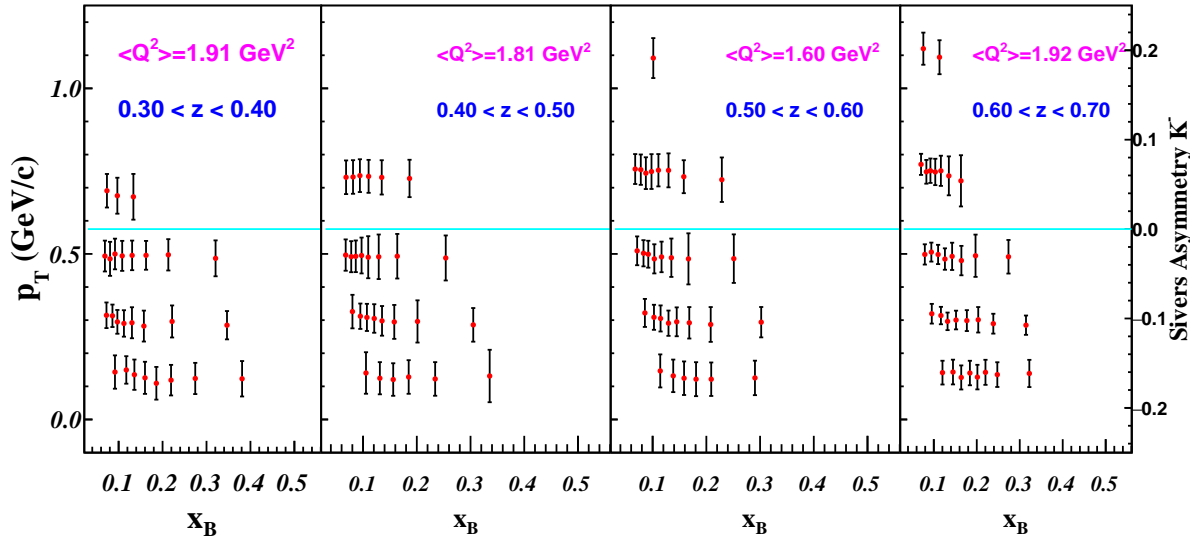


(b)  $\bar{p}(e, e'K^-)X$

Figure 27: The 3D ( $z$ ,  $p_T$ ,  $x_B$ ) binning projection and statistical uncertainties of the  $K^\pm$  Collins asymmetry ( $A_{UT}^{\sin(\phi+\phi_S)}$ ) for the transversely polarized  $\text{NH}_3$  (proton) target after combining the 11 GeV and 8.8 GeV simulation data. The sizes of the uncertainties are indicated by the Y axis on the right.



(a)  $\bar{p}(e, e'K^+)X$



(b)  $\bar{p}(e, e'K^-)X$

Figure 28: The 3D ( $z$ ,  $p_T$ ,  $x_B$ ) binning projection and statistical uncertainties of the  $K^\pm$  Siverts asymmetry ( $A_{UT}^{\sin(\phi-\phi_S)}$ ) for the transversely polarized  $\text{NH}_3$  (proton) target after combining the 11 GeV and 8.8 GeV simulation data. The sizes of the uncertainties are indicated by the Y axis on the right.

564 **4.4 Systematic Uncertainties**

		${}^3\text{He}$ ("n")		$\text{NH}_3$ ("p")	
Sources	Type	Collins ( $K^\pm$ )	Sivers ( $K^\pm$ )	Collins ( $K^\pm$ )	Sivers ( $K^\pm$ )
Raw Asymmetry	absolute	1.4E-3	1.4E-3	6.5E-3	6.5E-3
Background Subtraction	relative	1.0%	1.0%	2.0%	2.0%
Detector Resolution	relative	<1.0%	<1.0%	<1.0%	<1.0%
Nuclear Effect	relative	4.0% ~ 5.0%	4.0% ~ 5.0%	—	—
Diffractive Vector Meson	relative	<1.0%	<1.0%	<1.0%	<1.0%
Radiative Correction	relative	2.0 ~ 3.0%	2.0 ~ 3.0%	2.0 ~ 3.0%	2.0 ~ 3.0%
Target Polarization	relative	3.0%+0.5%	3.0%+0.5%	3.0%+0.5%	3.0%+0.5%
Total	relative	6 ~ 7%	6 ~ 7%	4 ~ 5%	4 ~ 5%

Table 2: Systematic uncertainties on separating Collins and Sivers asymmetries from the kaon-SIDIS production with the polarized  ${}^3\text{He}$  and  $\text{NH}_3$  targets.

565 A dedicated detector system for the approved pion SoLID-SIDIS experiments [19,20,33] has been designed  
 566 and will allow us to efficiently control the experimental related systematic uncertainties. In the last couple  
 567 of years, the SoLID-SIDIS configuration has been continuously optimized to reach the experimental require-  
 568 ments. The full  $2\pi$  azimuthal angular acceptance plays a huge role in reducing the systematic uncertainties  
 569 during the extraction of different azimuthal asymmetries. The frequently rotating target spin orientation will  
 570 also further suppress systematic uncertainties. The large signal-to-noise ratio, the high performance of the  
 571 modern particle detectors, as well as strong expertise in data analysis from the 6 GeV Hall-A Transversity  
 572 experiment and the CLAS experiment, will also help us to control the overall systematic uncertainty.

573 A good description of how to extract the physics results and control the systematic uncertainties was  
 574 given in our pion SIDIS proposals which in principle can be directly applied to our kaon-SIDIS experiment.  
 575 Nevertheless, we adopted the list of systematic uncertainties presented in the approved SoLID-SIDIS exper-  
 576 iments, and their updated values base on our new study given in the SoLID-pCDR and later work. These  
 577 uncertainties are given in Table 2.

578 We also consider the additional sources dedicated to the  $K^\pm$  measurements. Section 3.7 shows a 1%  
 579 or better contamination with a 20 ps time resolution before considering the background effect. To be  
 580 conservative, we assign a 3% systematic uncertainty due to the pion contamination.

581 **5 Summary**

582 We are proposing the measurement of  $K^\pm$  production in SIDIS with both the transversely polarized  ${}^3\text{He}$   
 583 as effective neutron targets and transversely polarized  $\text{NH}_3$  as proton targets. The experiment will run  
 584 in parallel with the approved  $\pi^\pm$ -SIDIS experiments, E12-10-006 and E12-11-108, using the same SoLID-  
 585 SIDIS configuration without modification. We will perform  $\pi^\pm/K^\pm$  separation using the PID cuts on the  
 586 MRPC-TOF distributions and the Heavy-Gas Čerenkov Detector signals during the offline analysis. The  
 587 high luminosity and large acceptance features of the SoLID allow us to simultaneously extract the  $K^\pm$  Collins  
 588 asymmetry, Sivers asymmetry and maybe other TMD asymmetries.

589 Our only extra requirement is to extend the performance of the MRPC detectors to provide a time  
 590 resolution of 20 ps for large-momentum kaons identification. We have proved that such a requirement

591 is reasonable and existing MRPC R&D projects have already achieved close or better timing resolution,  
592 although SoLID's high-rate environment will make the precise time measurement challenge. We also argued  
593 that even a slightly worse time resolution (30 ps) due to the high background rates still can help us to detect  
594  $K^\pm$  up to 6  $GeV/c$  and has very minimum impact to the physics projection.

595 Our new measurements will hence provide precise kaon SIDIS data that can help us to cleanly isolate  
596  $u$  and  $d$  quarks by combining with our pion SIDIS data. The new data will also provide unique sensitivity  
597 to the sea-quark TMDs and provide important theoretical and experimental guidance to the future SIDIS  
598 experiments on EIC which will perform precise measurements on the TMDs of sea-quarks and gluons.

## 599 References

- 600 [1] K. G. Wilson, *Phys. Rev. D* **10**, 2445 (1974).
- 601 [2] C. D. Roberts and A. G. Williams, *Prog. Part. Nucl. Phys.* **33**, 477 (1994).
- 602 [3] S. J. Brodsky, G. F. de Teramond, H. G. Dosch and J. Erlich, *Phys. Rep.* **584**, 1 (2015).
- 603 [4] J. Ashman *et al.* [European Muon Collaboration], *Phys. Lett. B* **206**, 364 (1988).
- 604 [5] J. Ashman *et al.* [European Muon Collaboration], *Nucl. Phys. B* **328**, 1 (1989).
- 605 [6] J. J. Ethier, N. Sato and W. Melnitchouk, *Phys. Rev. Lett.* **119**, no. 13, 132001 (2017).
- 606 [7] N. Sato *et al.* [Jefferson Lab Angular Momentum Collaboration], *Phys. Rev. D* **93**, no. 7, 074005 (2016).
- 607 [8] D. de Florian, R. Sassot, M. Stratmann and W. Vogelsang, *Phys. Rev. Lett.* **113**, no. 1, 012001 (2014).
- 608 [9] J. C. Collins, *Nucl. Phys. B* **396**, 161 (1993).
- 609 [10] S. J. Brodsky, D. S. Hwang and I. Schmidt, *Phys. Lett. B* **530**, 99 (2002).
- 610 [11] S. J. Brodsky, D. S. Hwang and I. Schmidt, *Nucl. Phys. B* **642**, 344 (2002).
- 611 [12] J. C. Collins, *Phys. Lett. B* **536**, 43 (2002).
- 612 [13] D. W. Sivers, *Phys. Rev. D* **43**, 261 (1991).
- 613 [14] T. Liu, Z. Zhao and H. Gao, *Phys. Rev. D* **97**, no. 7, 074018 (2018).
- 614 [15] A. Bacchetta, F. Conti and M. Radici, *Phys. Rev. D* **78**, 074010 (2008).
- 615 [16] J. She, J. Zhu and B. Q. Ma, *Phys. Rev. D* **79**, 054008 (2009).
- 616 [17] C. Lorce and B. Pasquini, *Phys. Lett. B* **710**, 486 (2012).
- 617 [18] T. Liu and B. Q. Ma, *Phys. Lett. B* **741**, 256 (2015).
- 618 [19] Approved SoLID SIDIS experiment E12-10-006, "Target Single Spin Asymmetry in Semi-Inclusive Deep-  
619 Inelastic ( $e, e'\pi^\pm$ ) Reaction on a Transversely Polarized  $^3\text{He}$  Target at 11 GeV", [https://www.jlab.org/  
620 exp\\_prog/proposals/14/E12-10-006A.pdf](https://www.jlab.org/exp_prog/proposals/14/E12-10-006A.pdf).

- 621 [20] Approved SoLID SIDIS experiment E12-11-108, “Target Single Spin Asymmetry in Semi-Inclusive Deep-  
622 Inelastic ( $e, e'\pi^\pm$ ) Reactions on a Transversely Polarized Proton Target”,  
623 [https://www.jlab.org/exp\\_prog/proposals/11/PR12-11-108.pdf](https://www.jlab.org/exp_prog/proposals/11/PR12-11-108.pdf).
- 624 [21] Approved SBS SIDIS experiment E12-09-018, “Measurement of Semi-Inclusive Pion and Kaon electro-  
625 production in the DIS Regime on a Transversely Polarized  $^3\text{He}$  Target using the Super BigBite and BigBite  
626 Spectrometers in Hall A”, <http://hallaweb.jlab.org/collab/PAC/PAC38/E12-09-018-SIDIS.pdf>.
- 627 [22] Conditionally approved CLAS12 SIDIS experiment C12-11-111, “Transverse spin effects in SIDIS at  
628 11 GeV with a transversely polarized target using the CLAS12 Detector”, [https://www.jlab.org/exp\\_](https://www.jlab.org/exp_prog/proposals/12/C12-11-111.pdf)  
629 [prog/proposals/12/C12-11-111.pdf](https://www.jlab.org/exp_prog/proposals/12/C12-11-111.pdf).
- 630 [23] A. Airapetian *et al.* [HERMES Collaboration], *Phys. Lett. B* **693**, 11 (2010).
- 631 [24] C. Adolph *et al.* [COMPASS Collaboration], *Phys. Lett. B* **744**, 250 (2015).
- 632 [25] X. Qian *et al.* [Jefferson Lab Hall A Collaboration], *Phys. Rev. Lett.* **107**, 072003 (2011).
- 633 [26] Y. X. Zhao *et al.* [Jefferson Lab Hall A Collaboration], *Phys. Rev. C* **90**, no. 5, 055201 (2014).
- 634 [27] A. Bacchetta, U. D’Alesio, M. Diehl and C. A. Miller, *Phys. Rev. D* **70**, 117504 (2004).
- 635 [28] A. Bacchetta, M. Diehl, K. Goeke, A. Metz, P. J. Mulders and M. Schlegel, *J. High Energy Phys.* **02**  
636 (2007) 093.
- 637 [29] M. Diehl and S. Sapeta, *Eur. Phys. J. C* **41**, 515 (2005).
- 638 [30] M. Boglione, J. Collins, L. Gamberg, J. O. Gonzalez-Hernandez, T. C. Rogers and N. Sato, *Phys. Lett.*  
639 *B* **766**, 245 (2017).
- 640 [31] T. C. Rogers, Mapping the partonic kinematics of semi-inclusive deep inelastic scattering, in prepare;  
641 and private communications.
- 642 [32] SoLID Collaboration, “Solenoidal Large Intensity Device Preliminary Conceptual Design Report”,  
643 [http://hallaweb.jlab.org/12GeV/SoLID/download/doc/solid\\_precdr\\_2017.pdf](http://hallaweb.jlab.org/12GeV/SoLID/download/doc/solid_precdr_2017.pdf).
- 644 [33] Approved SoLID SIDIS experiment E12-11-007, “Asymmetries in Semi-Inclusive Deep-Inelastic ( $e, e'\pi^\pm$ )  
645 Reactions on a Longitudinally Polarized  $^3\text{He}$  Target at 8.8 and 11 GeV”, [https://www.jlab.org/exp\\_](https://www.jlab.org/exp_prog/PACpage/PAC37/proposals/Proposals/New%20Proposals/PR-11-007.pdf)  
646 [prog/PACpage/PAC37/proposals/Proposals/New%20Proposals/PR-11-007.pdf](https://www.jlab.org/exp_prog/PACpage/PAC37/proposals/Proposals/New%20Proposals/PR-11-007.pdf).
- 647 [34] Approved SoLID  $J/\psi$  experiment E12-12-006A, “Near Threshold Electroproduction of  $J/\psi$  at 11 GeV”,  
648 [https://www.jlab.org/exp\\_prog/proposals/12/PR12-12-006.pdf](https://www.jlab.org/exp_prog/proposals/12/PR12-12-006.pdf).
- 649 [35] Approved SoLID SIDIS experiment E12-10-006A, “Dihadron Electroproduction in DIS with Trans-  
650 versely Polarized  $^3\text{He}$  Target at 11 and 8.8 GeV”, [https://www.jlab.org/exp\\_prog/proposals/14/](https://www.jlab.org/exp_prog/proposals/14/E12-10-006A.pdf)  
651 [E12-10-006A.pdf](https://www.jlab.org/exp_prog/proposals/14/E12-10-006A.pdf).
- 652 [36] Approved SoLID SIDIS experiment E12-11-108A, “Target Single Spin Asymmetry Measurements in  
653 the Inclusive Deep-Inelastic  $\vec{N}(e, e')$  Reaction on Transversely Polarized Proton and Neutron ( $^3\text{He}$ ) Tar-  
654 gets using the SoLID Spectrometer”, [https://www.jlab.org/exp\\_prog/proposals/14/E12-11-108A\\_](https://www.jlab.org/exp_prog/proposals/14/E12-11-108A_E12-10-006A.pdf)  
655 [E12-10-006A.pdf](https://www.jlab.org/exp_prog/proposals/14/E12-11-108A_E12-10-006A.pdf).



- 656 [37] Approved SoLID PVDIS experiment E12-10-007, “Precision Measurement of Parity-violation in Deep In-  
657 elastic Scattering Over a Broad Kinematic Range”, [https://www.jlab.org/exp\\_prog/PACpage/PAC37/  
658 proposals/Proposals/Previously%20Approved/E12-10-007.pdf](https://www.jlab.org/exp_prog/PACpage/PAC37/proposals/Proposals/Previously%20Approved/E12-10-007.pdf).
- 659 [38] Approved SoLID GPD experiment E12-10-006B, “Measurement of Deep Exclusive  $\pi^\pm$  Production using  
660 a Transversely Polarized  $^3\text{He}$  Target and the SoLID Spectrometer”, [https://www.jlab.org/exp\\_prog/  
661 proposals/17/E12-10-006B.pdf](https://www.jlab.org/exp_prog/proposals/17/E12-10-006B.pdf).
- 662 [39] Y. Wang *et al.*, “A MRPC prototype for SOLID-TOF in JLab,” *JINST* **8**, P03003 (2013).
- 663 [40] ALICE Collaboration, “The ALICE experiment at the CERN LHC”, *JINST* **3** (2008) S08002
- 664 [41] S. An, *et al.*, *Nucl. Instrum. Meth.* A594 (2008) 39-43
- 665 [42] L. Doroud, *et al.*, *Nucl. Instrum. Meth.* A629 (2011) 106-110
- 666 [43] Crispin Williams, *et. al.*, [https://indico.cern.ch/event/13750/contributions/146271/  
667 attachments/113687/161504/williams-alice\\_tof.pdf](https://indico.cern.ch/event/13750/contributions/146271/attachments/113687/161504/williams-alice_tof.pdf)
- 668 [44] EIC RD2013-5, “R&D Proposal for (Sub) 10 Picosecond Timing Detectors at the EIC”. [https://wiki.  
669 bnl.gov/conferences/images/3/38/PSTOF\\_EIC\\_July2014.pdf](https://wiki.bnl.gov/conferences/images/3/38/PSTOF_EIC_July2014.pdf)
- 670 [45] Fuyue Wang, Dong Han, Yi Wang, Yancheng Yu, Baohong Guo, and Yuanjing Li, ”A neural network  
671 based algorithm for MRPC time reconstruction.”, arXiv:1805.02833
- 672 [46] W. Riegler, *et al.*, *Nucl. Instrum. Meth.* A500 (2003) 144-162
- 673 [47] S. Ramo, *Proc.Ire.* 27 (1939) 584-585
- 674 [48] Z. Ye, N. Sato, K. Allada, T. Liu, J-P Chen, H. Gao, Z. Kang, A. Prokudin, P. Sun, and F. Yuan, *Phys.*  
675 *Lett. B* **767**, 91 (2017).
- 676 [49] GetSIDIS, a SIDIS Monte Carlo Generator, <https://github.com/yezhihong/GetSIDIS>.
- 677 [50] A. Accardi, L. T. Brady, W. Melnitchouk, J. F. Owens and N. Sato, *Phys. Rev. D* **93**, no. 11, 114017  
678 (2016), <https://www.jlab.org/theory/cj/index.html>.
- 679 [51] D. de Florian, R. Sassot and M. Stratmann, *Phys. Rev. D* **75**, 114010 (2007).